Coherent nanoscale imaging and chemical mapping with compact extreme ultraviolet and soft x-ray sources: Review and perspective

Cite as: APL Photon. 10, 050901 (2025); doi: 10.1063/5.0254017
Submitted: 20 December 2024 • Accepted: 14 April 2025 •
Published Online: 19 May 2025

W. Eschen,[1,2,3,a)] R. Klas,[1,2,3,4] D. S. Penagos Molina,[1,2,3] S. Fuchs,[1,2,5,6] G. G. Paulus,[1,2,5] J. Limpert,[1,2,3,4] and J. Rothhardt[1,2,3,4]

AFFILIATIONS

[1] Helmholtz-Institute Jena, Fröbelstieg 3, 07743 Jena, Germany
[2] GSI Helmholtzzentrum für Schwerionenforschung, Planckstraße 1, 64291 Darmstadt, Germany
[3] Institute of Applied Physics, Abbe Center of Photonics, Friedrich-Schiller-University Jena, Albert Einstein-Straße 15, 07745 Jena, Germany
[4] Fraunhofer Institute for Applied Optics and Precision Engineering, Albert-Einstein-Str. 7, 07745 Jena, Germany
[5] Friedrich Schiller University Jena, Institute of Optics and Quantum Electronics, Max-Wien-Platz 1, 07743 Jena, Germany
[6] University of Applied Sciences Mittweida, Laserinstitut (LHM), Technikumplatz 17, 09648 Mittweida, Germany

Note: This paper is part of the Special Topic on Advances Enabled by Ytterbium: From Advanced Laser Technology to Breakthrough Applications.
[a)] **Author to whom correspondence should be addressed:** wilhelm.eschen@uni-jena.de

ABSTRACT

Short-wavelength radiation in the extreme ultraviolet (XUV) and soft x-ray spectral regions offers unique advantages for imaging. With wavelengths ranging from a few nanometers to a few tens of nanometers, these techniques enable spatial resolutions at the nanometer scale. In addition, penetration depths in solids in this spectral regime enable non-destructive imaging of internal structures of micrometer-thick objects, surpassing the capabilities of electron microscopy. Furthermore, the diverse atomic absorption edges characteristic of this spectral region enable high-contrast imaging without any staining or labeling. When combined with quantitative phase-sensitive imaging techniques, even material identification at the nanoscale becomes feasible. This article reviews some of the latest advancements in the field. It provides an overview of the available tabletop sources in this spectral region and discusses concepts and state-of-the-art results of two complementary imaging techniques: XUV ptychography and XUV coherence tomography. While XUV ptychography achieves nanoscale lateral resolution, XUV coherence tomography enables nanoscale axial resolution. Both techniques allow for the non-destructive mapping of the chemical composition of samples, facilitating localized analysis of material compositions in integrated circuits or microorganisms. The article also presents a perspective on future developments in time-resolved and 3D XUV imaging and potential future application fields.

I. INTRODUCTION

Visualizing objects is essential for understanding and manipulating their properties. Therefore, microscopy is a fundamental cornerstone, enabling significant scientific and technological advancements. Short wavelength photons in the XUV and soft x-ray spectral regions (1–100 nm) provide unique opportunities for imaging with nanoscale resolution. These spectral regions feature a magnitude of absorption edges, which are characteristic for each chemical element, enabling label-free high-contrast and element-specific imaging. Moreover, within this spectral range, the attenuation length in matter typically spans a few to several tens of micrometers,

depending on the material composition and the specific photon energy. This property allows for non-destructive visualization of internal structures within complex samples.

While classical x-ray microscopes are typically limited in resolution due to the employed zone plate optics,[1–3] coherent diffractive imaging (CDI) techniques avoid the losses and aberrations of conventional optics by applying computational imaging methods instead. These techniques have been pioneered at synchrotron facilities and free-electron lasers over the past two decades and have demonstrated imaging performance beyond the capabilities of lens-based x-ray microscopy.[4–9]

At the same time, laser-driven short-wavelength sources have been developed, enabling lab-scale experiments that were previously exclusive to large-scale facilities. Especially, coherent short-wavelength sources based on high-order harmonic generation (HHG)[10] have recently gained attention.[11,12] HHG involves an extremely non-linear conversion of an ultra-fast driving laser to the XUV or soft x-ray range. Due to the phase-locked nature of this process with the driving laser, HHG results in spatially coherent radiation.[13] Consequently, this has enabled the transfer of short-wavelength coherent imaging techniques to compact, laboratory-scale setups.[14] Particularly ptychography,[15–18] which is a scanning version of CDI,[19] is ideally suited for XUV and soft x-ray microscopy, as this method enables amplitude and phase contrast with high lateral resolution. In combination with HHG sources, ptychography is now being explored by a growing number of research groups worldwide, predominantly for high-resolution imaging of complex samples from a broad range of fields and for high-resolution XUV wavefront-sensing applications.[20,21]

Complementary to ptychography, XUV and soft x-ray coherence tomography (XCT)[22] have been developed in recent years, which are essentially extensions of established optical coherence tomography[23,24] to shorter wavelengths. XCT leverages the spectral bandwidth of an XUV or soft x-ray source to directly image the axial dimension of a sample in reflection geometry. Combined with lateral scanning, XCT provides non-destructive three-dimensional tomograms with an axial resolution down to a few nanometers. Due to its broadband imaging scheme, XCT is particularly well-suited for intrinsically broadband high harmonic sources and provides both structural and spectroscopic information about the sample simultaneously.

Notably, both ptychography and XCT enable the identification of different materials within recorded images due to the characteristic strong elemental contrast in the XUV and soft x-ray spectral regions. This enables quantitative mapping of chemical composition at the nanoscale with unique sensitivity, particularly for light elements. Combined with the penetrating power of short-wavelength radiation, these techniques can reveal the internal structure and composition of complex samples, even for cases that are hard to access with other methods.

In this article, the current state-of-the-art in this field and a perspective on future developments and applications are provided. Section II provides an overview of the currently available compact XUV and soft x-ray sources, including a comparison of their brightness and coherent power and an emphasis on HHG sources. In Sec. III, HHG-driven ptychography is discussed. This section includes a basic introduction to ptychography as well as a review of recently introduced methods for increasing image quality and improving material identification. Section IV discusses XCT, a technique for non-destructive chemical mapping with nanoscale axial resolution. The section includes an overview of the XCT method and reviews recent studies of cross-sectional chemically mapped samples. In Sec. V, current challenges, trends, future opportunities, and potential application fields will be discussed, followed by a summary in Sec. VI.

II. COMPACT EXTREME ULTRAVIOLET AND SOFT X-RAY SOURCES

In this section, the most prominent short-wavelength sources are discussed, and their suitability for nanoscale coherent imaging modalities is evaluated. Coherent diffractive imaging techniques, such as ptychography, require monochromatic radiation. In contrast, XCT demands a broadband or tunable spectrum to retrieve depth information. Despite this difference, both methods benefit from a high photon flux and a high degree of spatial coherence. Here, short wavelength sources are compared by the spectral average brightness B_s^{avg}, defined as[25]

$$B_s^{\mathrm{avg}} = \frac{\Phi_{\mathrm{avg}}}{\Sigma_x \Sigma_y \Sigma_{\theta_x} \Sigma_{\theta_y}} \frac{1}{\Delta E/E},$$

with the average photon flux Φ_{avg}, and the source size $\Sigma_{x,y}$ and the divergence $\Sigma_{\theta_x,\theta_y}$ in the x- and y-directions, respectively, $\Delta E/E$ corresponds to the relative bandwidth.[26] Using this metric, different XUV and SXR sources can be compared as shown in Fig. 1. Notably, there is a relation between the average brightness and the coherent power emitted by a given source (indicated by the right y axis in Fig. 1).

Coherent nanoscale imaging techniques have been pioneered at synchrotrons.[47–49] Currently, third-generation synchrotrons are the workhorses for nanoscale imaging in the soft- and hard x-ray spectral regions. These sources are based on large high-energy electron storage rings with up to hundreds of meters of circumference.[50] Typical synchrotron facilities offer multiple beamlines that can be used to conduct experiments in parallel. The brightness of some of the most powerful synchrotrons is indicated in Fig. 1. Recently, the first fourth-generation synchrotrons have become operational, with many more currently being planned and commissioned. These facilities offer exceptionally high coherence and significantly greater average brightness, enabling higher resolution and faster imaging.[51]

In contrast to a synchrotron, free-electron lasers (FELs) typically rely on linear accelerators. The lengths of these facilities can extend to several kilometers. The average brightness is two to three orders of magnitude higher than that of any other light source type (Fig. 1). In addition to the outstanding average brightness, FELs also show extremely high peak brightness.[52] This enables single-shot imaging experiments, where the sample diffracts the incoming radiation before it gets destroyed due to the high dose.[53] However, compared to other sources, FELs are rare and exhibit large costs for construction, maintenance, and operation. Furthermore, the linear design allows for only a limited number of beamlines that can be used simultaneously.

To enable coherent nanoscale imaging experiments on a laboratory scale, complementary compact and high-brightness sources are desired. Currently, state-of-the-art tabletop sources predominantly rely on laser-driven processes (Fig. 1). Examples include

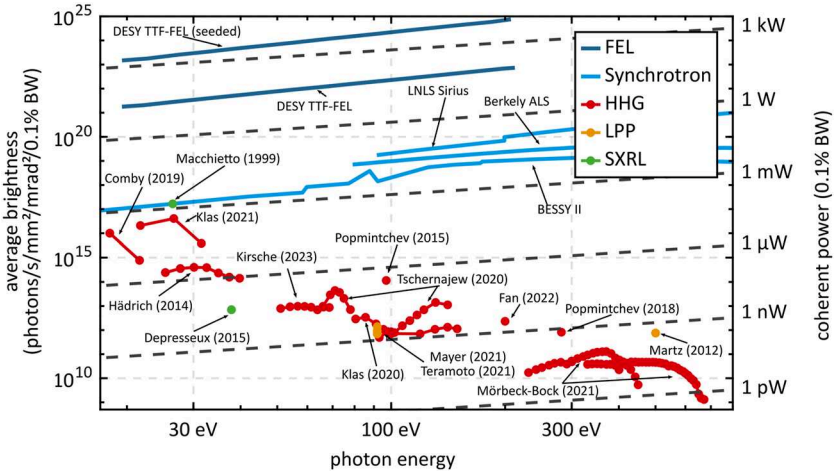

FIG. 1. Average brightness of selected state-of-the-art XUV and soft x-ray sources vs photon energy. The data include large-scale facilities, such as synchrotrons[27–29] and free-electron lasers (FELs),[30] as well as tabletop sources, such as HHG,[31–41] laser-produced plasma (LPP),[42–44] and soft x-ray lasers (SXRLs).[45,46] The dashed isoclines correspond to the coherent power in a 0.1% bandwidth.

laser-produced plasma sources,[54] higher-order harmonic generation,[10] and soft x-ray lasers.[55] At low photon energies, these sources are competitive with synchrotrons. However, their average brightness decreases with increasing photon energy (Fig. 1). The advantages of tabletop sources are their availability, low cost, and compact footprint.[56] Furthermore, these sources are portable and can be operated outside specialized laser laboratories. In the following, three different types of laboratory-scale XUV and SXR sources are discussed.

Laser-produced plasma (LPP) sources are incoherent light sources.[57] Typically, these sources are driven by laser pulses with energies of several hundred millijoules and pulse durations in the range of 10 nanoseconds. During irradiation of a target material, a high-charge-state plasma is generated. The XUV and SXR emissions are due to the black-body radiation and an incoherent addition of the characteristic lines of the emitters in the target material into a 2π semisphere.[58]

High-harmonic generation (HHG) is an alternative approach that allows for the generation of spatially coherent laser-like radiation,[13] making it ideal for nanoscale imaging. Such sources are currently the workhorse for most tabletop lensless imaging experiments.[20] In this process, a millijoule-class laser with pulse durations of a few tens of femtoseconds is focused with high peak intensity into a target.[59] Commonly, but not necessarily, the target is a noble gas. The laser interaction with the target atoms can be understood in a so-called three-step model.[60] (1) The atom is field ionized by the external laser field, (2) the now free electron is accelerated in the laser field, and (3) the electron returns to its parent ion and recombines with it while emitting the excess energy in the form of an XUV or SXR photon. The interaction of the laser-driven electron only with its parent ion dictates a well-defined phase relation between the emitted XUV photon and the driving laser. Furthermore, a coherent build-up of the generated XUV and SXR radiation can be achieved via transient phase-matching techniques.[11] Briefly, the entire process is coupled to the driving laser field. Hence, all laser properties (low divergence, high spatial coherence, and short pulse duration) are inherited into the XUV and SXR. The generated spectrum can be tailored by the driving laser parameters, delivering distinct narrowband lines up to continuous spectra spanning more than 100 eV of bandwidth.[61] Furthermore, it is possible to tune the narrow lines to desired photon energies.[40] Generally, the generated brightness decreases with increasing photon energies, which is inherent to the HHG process.[11] However, at photon energies below 30 eV, the brightness of these sources is comparable to large-scale facilities (Fig. 1).[33]

Until now, the full potential of HHG-driven sources has not been completely exploited. In the low energy region of sub-30 eV, the average brightness has experienced an exponential increase during the last few years. This has been achieved by different factors, including a cascaded frequency conversion for a higher conversion efficiency,[33] recycling of the driving laser using enhancement cavities,[37] or the upscaling of the average power of the driving laser systems.[12] In the future, this trend of increased average brightness can also be expected in the SXR region. Initial demonstrations of novel high-power laser systems have already demonstrated more than one order of magnitude higher average power than the driving lasers used for state-of-the-art HHG sources.[62–64] In conjunction with the optimization of driving wavelength for different targeted

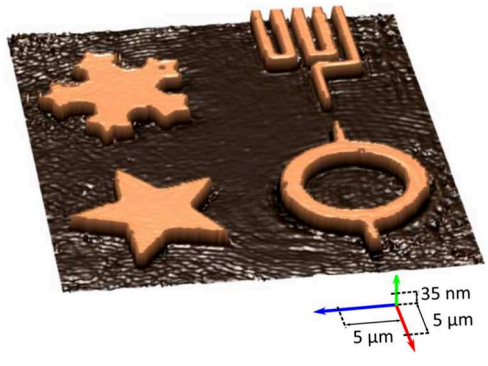

FIG. 2. Reconstructed height profile from the first XUV ptychography experiment conducted at a wavelength of 29.5 nm. The height profile was derived from the reconstructed phase. Reprinted with permission from Seaberg *et al.* Optica **1**, 39–44 (2014).[69] Copyright Optical Society of America.

XUV to SXR regions, an increase of the average brightness of up to three orders of magnitude appears feasible within the next years.

Furthermore, direct amplification of XUV to SXR radiation is possible using a soft x-ray laser (SXRL).[55] The active material for the amplification is a plasma, generated by a Joule-class laser with picosecond pulse duration. Hence, the spectrum consists of a narrow spectral line at a characteristic emission wavelength of the material used. SXRLs deliver the highest average brightness of table-top sources (Fig. 1). However, due to the complexity of the required laser systems, their appearance is rare compared to HHG-based sources. Nevertheless, these systems enable high-resolution conventional[65] and lensless imaging[66] in the XUV. Notably, the high XUV pulse energy allows for single-shot measurements.

III. XUV PTYCHOGRAPHY: NON-DESTRUCTIVE CHEMICAL MAPPING WITH NANOSCALE LATERAL RESOLUTION

A. Introduction

High-resolution microscopy in the short wavelength range is challenging due to difficulties in fabricating high-quality optics for this spectral range. This challenge can be overcome by modern computer-based coherent diffractive imaging (CDI) methods, where the object is numerically reconstructed from the measured diffraction pattern.[19] A special form of CDI is ptychography.[16–18] In its most basic implementation, a sample is raster-scanned by a localized beam, and a set of diffraction patterns is recorded for overlapping positions. The complex-valued transmission (i.e., amplitude and phase) of the object and complex-valued illumination—referred to as probe—are then numerically reconstructed from the diffraction data. Ptychography was initially devised as a computational method to solve the phase problem in electron diffraction.[67] It has since evolved into a widely used technique, particularly in the x-ray range at synchrotron facilities.[68]

However, ptychography in the XUV range is also very promising due to the presence of numerous electronic resonances across a wide range of elements. These resonances result in a diverse refractive index, providing rich amplitude and phase information that can be effectively probed with ptychography. When combined with the spatially coherent HHG sources introduced in Sec. II, high-resolution XUV imaging experiments at a laboratory scale are now feasible.

Ptychographic imaging in the XUV range using HHG sources has gained increasing attention in recent years. The first experiment successfully demonstrated XUV ptychography in a reflection geometry, highlighting its immense potential.[69] Notably, it was shown that the reconstructed phase of the object can be utilized to determine the sample's topography with deep sub-wavelength resolution (Fig. 2).

In later experiments, high-resolution imaging was demonstrated in a transmission geometry as well[70–72] with resolutions well below 20 nm.[71,72] Consequently, XUV ptychography has led to a wide range of applications, including imaging of critical lithography components[73–75] and high-resolution imaging of biological samples.[76,77] Furthermore, ptychography can be used as a high-resolution multi-wavelength XUV wavefront sensor[78] to gain insights into the generation of high-order harmonics[79–82] and to characterize XUV optics.[83]

Figure 3 shows a typical HHG-driven ptychography setup. Starting from the XUV generation, an ultrafast driving laser is focused into a gas jet to intensities of 10^{14} W/cm^2 to generate high-order harmonics. The HHG radiation is separated from the driving laser typically by grazing incident plates[84] (GIPs) and thin metal foils. Subsequently, the HHG beam is spectrally filtered and focused by XUV multilayer mirrors, after which a structured mask is used to constrain the beam and tailor the illumination. Behind the sample, a pixelated detector is placed to measure the diffraction pattern for each scanning position. The set of diffracted patterns is then numerically reconstructed, yielding the complex transmission of the sample and illuminating beam (referred to as a probe). However, ptychography imposes several strict requirements on the measurements. The most important ones are as follows:

- A stable ptychography setup is essential, meaning that the illumination must remain consistent in shape,

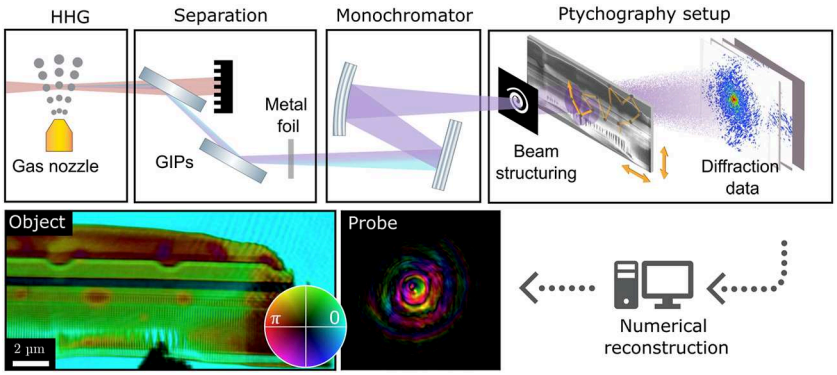

FIG. 3. Typical HHG-driven ptychography setup. The XUV radiation is generated by an ultra-short pulsed driving laser focused in a gas nozzle. Grazing incidence plates (GIPs) are placed after the gas jet to separate the XUV radiation from the driving laser. The XUV radiation is then spectrally filtered and focused by multilayer mirrors. A pinhole or mask is placed before the sample to constrain the illumination size and to tailor its wavefront. The diffraction is then recorded by a detector placed in the far-field of the sample. Finally, the complex-valued transmission of the sample and beam is obtained in a computer by an iterative phase retrieval algorithm. Reconstructed object and probe adapted from Eschen *et al.* Light Sci Appl **11**, 117 (2022).[72]

power, and position throughout the measurement.[85] Furthermore, precise knowledge of the scan positions is required.[86]
- Adjacent scan positions must overlap sufficiently. Typically, an overlap of more than 75% is chosen.[87]
- The illumination must fit within the numerical window defined by the detector's sampling.
- The sample must be sufficiently thin.[88]
- The illumination must be sufficiently spatially and temporally coherent.[89]

These requirements can be relaxed by using adapted ptychography models. For example, these models enable ptychography using broadband or partially coherent radiation[90,91] and allow the investigation of samples thicker than the depth of field.[92] The variety of these models and the need for GPU-optimized code make the numerical implementation of ptychography challenging for newcomers. For this reason, various open-source ptychography libraries have emerged in recent years.[93–95] For further details on these ptychography models and additional information on ptychography in general, reference is made here to a recent book chapter by Maiden and Rodenburg, which describes ptychography in detail.[96] This perspective discusses typical challenges for tabletop XUV ptychography with HHG sources and material-specific ptychography in more detail.

B. Challenges for tabletop XUV ptychography

This section discusses three crucial challenges that arise in XUV ptychography when employing laser-driven HHG sources: XUV ptychography in the presence of instabilities, the shaping of structured XUV beams, and the use of broadband radiation for XUV ptychography.

1. XUV ptychography in the presence of instabilities

Ptychography requires stable illumination regarding power, position, and wavefront; otherwise, the overlap between neighboring positions is no longer sufficiently defined, and reconstructions might fail. However, generating stable HHG beams is not trivial, since the generation of high-order harmonics is an extremely non-linear process,[97] meaning that even slight fluctuations in the driving laser can lead to significant instabilities in the generated high-harmonic radiation. Furthermore, thermal drifts of the optical components in the beam path up to the sample can lead to slow changes of the illumination during long ptychography scans. Therefore, this section discusses the impact of instabilities on image quality and strategies for improving image quality in the presence of instabilities. These instabilities can be categorized into two types.

The first type of instability arises from changes occurring at a characteristic time faster than the exposure time (i.e., fast vibrations, Fig. 4(a)). This leads to an incoherent sum of slightly

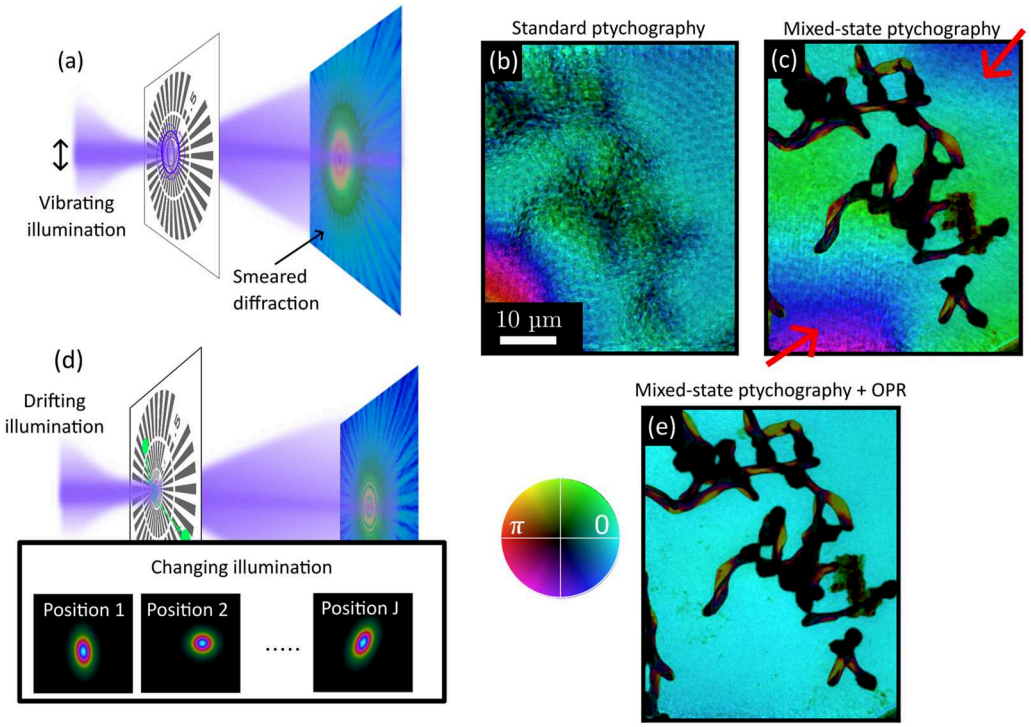

FIG. 4. (a) Schematic illustration of ptychography affected by fast instabilities (e.g., vibrations), resulting in a smeared diffraction pattern. (b) Reconstruction of A. nidulans germlings using a standard algorithm in the presence of fast instabilities. (c) Reconstruction of the same dataset using mixed-state ptychography, significantly improving image quality. (d) Schematic illustration of slow instabilities, effectively causing variations in illumination at each position. (e) Reconstruction of the A. nidulans dataset using a combination of mixed-state ptychography and OPR, further enhancing image quality.

different diffraction patterns, leading to a smeared diffraction pattern with reduced fringe contrast. Consequently, such diffraction patterns are similar to those acquired with a partially coherent source. High-quality reconstruction can be achieved even under partially coherent conditions using mixed-state ptychography,[90] an extension of the classical ptychography algorithm. Accordingly, mixed-state ptychography can be employed to compensate for fast oscillations of the object or illumination.[98] Here, this is visualized using an XUV ptychography measurement of a microbiological specimen where significant vibrations are present.[77] Figure 4(b) shows the corresponding ptychography reconstruction using a standard ptychography algorithm without mixed-state implementation. Artifacts dominate the resulting reconstruction. In contrast, the reconstruction with mixed-state ptychography shows significantly higher image quality [Fig. 4(c)]. However, an inhomogeneous phase background (indicated by red arrows) is still visible in the reconstruction. This phase background is not part of the investigated sample and arises from instabilities of the illumination that occur on timescales slower than the exposure time, which will be discussed below.

The second type of instabilities comprises drifts occurring over time scales comparable to or longer than the exposure time (e.g., thermal drifts). These drifts result in an illumination that varies for the different scan positions [Fig. 4(d)]. Traditional reconstruction algorithms do not accommodate these gradual illumination changes. To solve this issue, orthogonal probe relaxation (OPR) ptychography was developed.[85] In OPR, slight changes in the illumination are allowed, which is achieved by constraining the probe changes to a lower dimensional space using a truncated singular value decomposition (for more details, the reader is referred to the original publication[85]). This process ensures a controlled degree of similarity of the probe drift and allows high-quality reconstruction even under unstable experimental conditions. Applying OPR to the measurement in Fig. 4(c) eliminates additional artifacts, such as the inhomogeneous phase background, as demonstrated in Fig. 4(e). This is particularly important when quantitative information is to be obtained from the reconstructed phase and amplitude.

2. Shaping of XUV light fields

In recent years, highly structured beams have been identified as crucial for achieving high-quality ptychographic reconstructions.[99–101] This can be attributed to their broad spatial frequency spectrum and diverse real-space distribution. While structured beams present several benefits,[96] this discussion focuses on their two most significant advantages. First, the diverse real-space pattern of structured beams leads to stronger changes in the diffraction patterns as the object is scanned. This enhanced translation diversity not only contributes to more reliable numerical reconstructions but also minimizes the occurrence of artifacts.[100] Second, a broader angular illumination spectrum eases the detector's dynamic range requirements by distributing the diffraction pattern more evenly across the detector. This reduces the intensity of the central speckle, allowing more photons to be measured before reaching overexposure, while simultaneously enhancing the strength of larger diffraction angles relative to the zero order. These combined advantages lead to more robust reconstructions and higher spatial resolution.

In the x-ray domain, Fresnel zone plates are commonly used for focusing, providing a broad spatial frequency spectrum that facilitates the generation of customized illumination patterns.[100,102] In contrast, HHG-driven ptychography setups predominantly use multilayer mirrors, which serve the dual purpose of focusing and spectral selection. However, these optics often lead to smooth beams with a narrower angular spectrum, limiting the overall performance of HHG-driven ptychography.

Recently, two approaches have been developed to structure XUV beams for ptychography. The first approach is known as mask-based structured illumination ptychography. In this approach, a nanostructured mask is employed directly in front of the sample (commonly around 100 μm) to structure the illumination.[72,103] Figure 5(a) shows the unstructured beam generated by a simple pinhole mask. The corresponding reconstruction, shown in Fig. 5(b), tends to have low resolution and artifacts. Conversely, the second beam, illustrated in Fig. 5(c), created by a phase-shifting diffuser pattern (shown in the small inset), results in a highly structured beam. The reconstruction using this beam results in a significantly higher resolution, free of previously observed artifacts [Fig. 5(d)].

The second approach to generating structured XUV beams involves driving the HHG process with a structured beam, commonly employing orbital angular momentum (OAM) beams for this purpose.[105,106] Although this technique introduces additional complexity to the ultrafast laser system and the HHG process, it has recently been applied successfully for nanoscale imaging [Fig. 5(e)].[104] In this study, it was demonstrated that structured beams with a broad angular spectrum are crucial for imaging highly periodic structures, which are commonly encountered in the semiconductor industry. This was exemplified through the use of a highly structured XUV-OAM beam.

3. Ptychography using broadband XUV radiation

HHG radiation is typically broadband, comprising multiple harmonics or a broadband continuum. However, this broad spectrum conflicts with the temporal coherence requirements for lensless imaging since the broadband radiation leads to a blurring of the diffraction pattern.[89] Consequently, most of the time only a narrow bandwidth is selected, leaving the majority of the generated photons unused. At the same time, XUV ptychography with broadband HHG spectra provides a valuable opportunity to obtain spatially resolved spectroscopic images. Due to these advantages, XUV ptychography with broadband radiation is of particular interest in current research.

In recent years, several methods have been developed to enable lensless imaging with broadband HHG sources [Fig. 6(a)].[91,107,108] The two most common methods are ptychographic information multiplexing (PIM)[91] and numerical monochromatization of the diffraction patterns.[108–110] PIM extends classical ptychography to reconstruct multiple objects and illuminations for varying wavelengths. This method has the advantage of enabling the study of dispersive samples (e.g., covering an absorption edge) as well as wavelength-dependent illuminations [Fig. 6(b)]. In the second method, the monochromatic diffraction patterns are computed from the measured broadband diffraction patterns [Fig. 6(c)]. Subsequently, the object and illumination are reconstructed using a conventional ptychography algorithm; therefore, a specialized

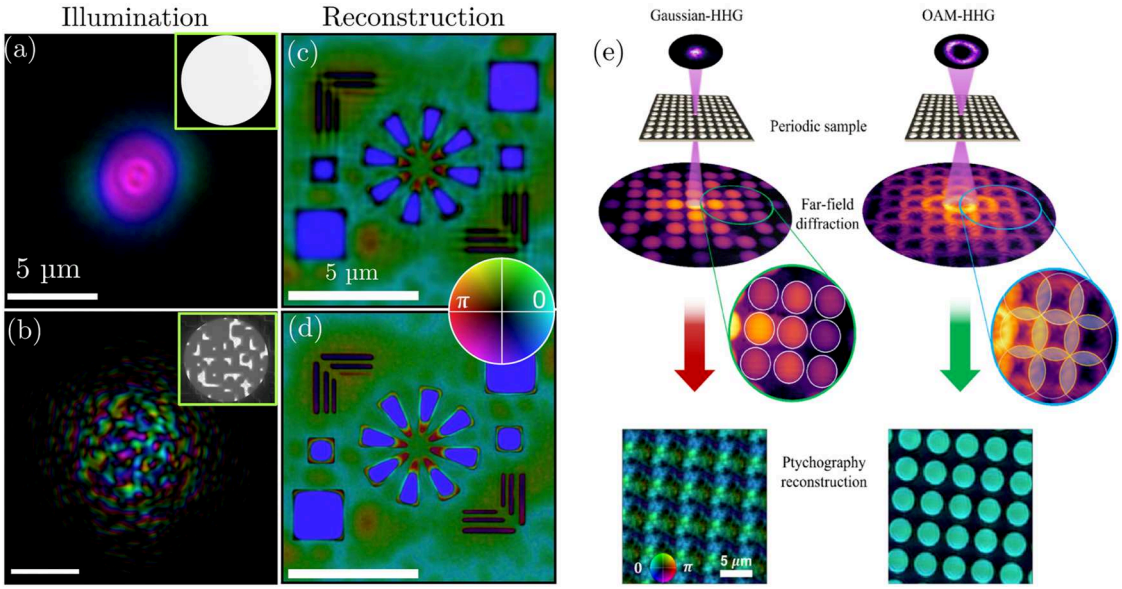

FIG. 5. (a) Unstructured XUV beam created by a pinhole aperture with its SEM image displayed in the inset. (b) Structured XUV beam created by a phase-shifting diffuser with its SEM image displayed in the inset. (c) Ptychography reconstruction of a test sample illuminated with the unstructured beam shown in (a). (d) Ptychography reconstruction of the same test sample but illuminated with the structured beam shown in (b). (e) The use of HHG-OAM beams, which are highly structured and exhibit a broad angular spectrum, leads to more robust and reliable reconstructions of periodic samples. (a)–(d) adapted from Eschen *et al.* Opt. Express **32**, 3480–3491 (2024).[103] Copyright 2024 Author(s), licensed under a Creative Commons Attribution 4.0 License. (e) Reprinted with permission from Wang *et al.* Optica **10**, 1245–1252 (2023).[104] Copyright Optica Publishing Group.

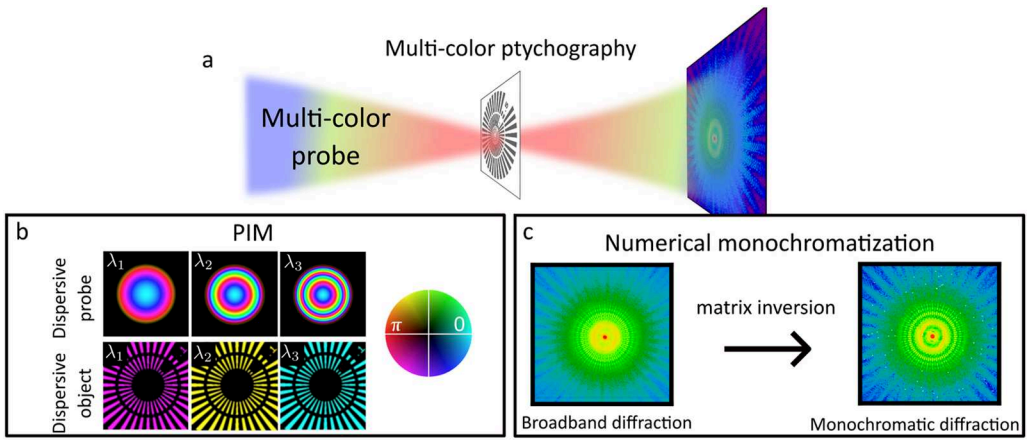

FIG. 6. (a) Schematic representation of ptychography with multiple wavelengths. (b) Reconstruction using the ptychographic information multiplexing algorithm (PIM), which enables the reconstruction of dispersive objects and illuminations (probes). (c) Illustration of numerical monochromatization of the measured broadband diffraction patterns. The monochromatic diffraction pattern is computed from the broadband diffraction under the assumption that both the object and the exposure function are achromatic.

reconstruction algorithm is not required. This method is usually referred to as numerical monochromatization. However, it fails for dispersive objects and illuminations that are highly wavelength-dependent.

In recent years, PIM has been used primarily for broadband XUV ptychography, demonstrating that spectroscopic sample information can be obtained from a single ptychography measurement.[78] Furthermore, PIM enables high-resolution retrieval of the spectrally resolved illumination wavefront. For instance, the PIM algorithm has been employed to investigate the spatiotemporal properties of HHG beams.[79,81] In this context, the spectrally resolved wavefronts of harmonics ranging from the 15th to the 25th

order were characterized (Fig. 7).[79] The study revealed that different harmonics exhibit significantly varying wavefronts, which can introduce chromatic aberrations, potentially impacting attosecond experiments.

Ptychographic reconstructions using PIM are typically significantly more challenging than under monochromatic conditions, as spectral information must be reconstructed. This is usually achieved by increasing the scan overlap, which results in longer measurement times. Notably, comb-like spectra are generally easier to reconstruct than broad continua, which are required for attosecond pulses.[111] However, PIM has also been successfully demonstrated using a broad spectral continuum by using an extremely high scan overlap.[112]

Unlike the PIM algorithm, numerical monochromatization of the diffraction patterns is particularly suitable for continuous spectra when the illumination (probe) and the object are sufficiently achromatic. This is especially promising for the soft x-ray range, where HHG sources typically exhibit a lower photon flux, allowing more photons to be utilized.[111]

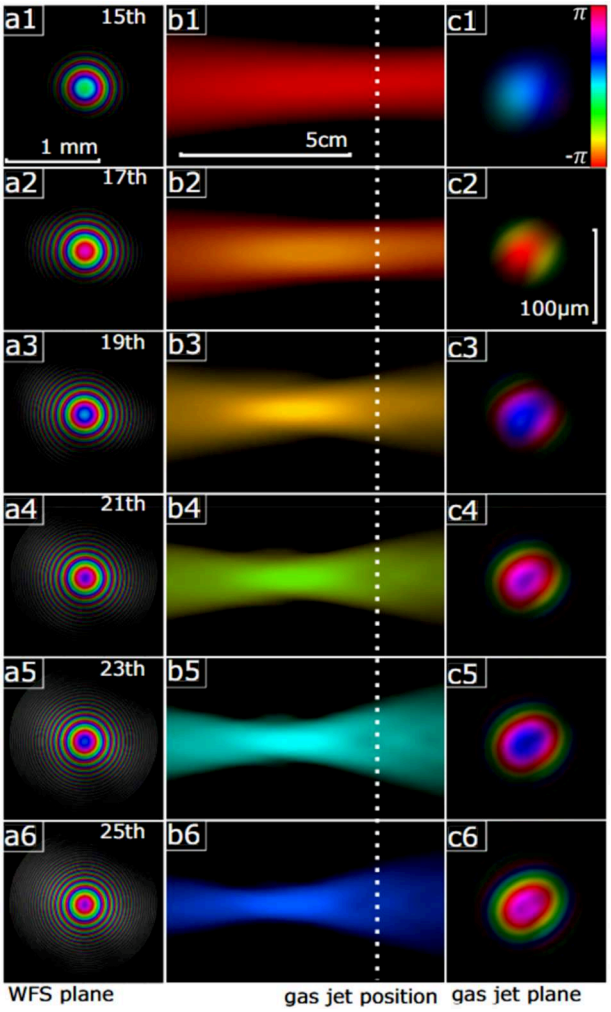

FIG. 7. Reconstructed spectrally resolved wavefront of an HHG comb containing six harmonic orders, ranging from 55 nm (15th harmonic) to 33 nm (25th harmonic). The left column (a1)–(a6) displays the reconstructed wavefront in the plane where the object was placed. The middle column (b1)–(b6) presents an axial cross section of the reconstructed beam, with the white dashed line indicating the gas jet position. The right column (c1)–(c6) shows the reconstructed beam in the gas jet plane. Adapted from Liu *et al.* Phys. Rev. Research **5**, 043100 (2023). Copyright 2023 Author(s), licensed under a Creative Commons Attribution 4.0 License.

C. Chemical mapping with XUV ptychography

XUV ptychography is ideally suited for obtaining material-specific information with high resolution. This is because the refractive index n is particularly diverse in the XUV spectral range and can be formulated as[25]

$$n = 1 - \frac{r_e \lambda^2}{2\pi} n_a (f_1 + i f_2).$$

Here, r_e represents the classical electron radius, n_a denotes the atomic number density, and f_1 and f_2 are the real and imaginary components of the atomic scattering factor, respectively. The atomic scattering factor describes the scattering of atoms relative to a free electron. Consequently, f_1 and f_2 are significantly influenced by various atomic resonances within atoms. This relationship is illustrated by Fig. 8, which depicts the atomic scattering factor for all elements within the energy range of 30–1000 eV. Since almost all elements exhibit electronic resonances (e.g., K, L, M edges) in this spectral range, the resulting refractive index shows a lot of diversity in this spectral range, rendering it highly effective for chemically sensitive imaging. Ptychography, in particular, is exceptionally well-suited for such analyses, as it reconstructs the object's complex-valued response, thereby providing more information on the sample's composition compared to amplitude-only imaging modalities.

Several methods for reflection and transmission measurements have been developed to extract information about the material composition from the complex-valued reconstructed object. In transmission measurements, the reconstructed amplitude and phase can be utilized to calculate the scattering quotient,[114] defined by $f_q = f_1/f_2$. This quotient, unaffected by the sample's thickness, offers a material-specific signature. The basic principle was demonstrated on a HHG-driven ptychography setup using a lamella of highly integrated circuited extracted from a conventional flash memory.[72] The calculated scattering quotient map is shown in Fig. 9(a) and enables the identification of materials like aluminum, silicon oxide, and silicon nitride, which are common for this device. The same technique can also be applied to more complex samples, such as microorganisms, providing valuable insights into their ultrastructure.[77]

Interpreting the complex-valued reconstructed object function in reflection ptychography measurements presents additional challenges. The reconstructed amplitude and phase are influenced by various factors such as material composition, surface roughness, topography, and layer structure. However, this dependency also provides an opportunity to characterize these parameters non-destructively and with high spatial resolution.[73,116,117] Nonetheless,

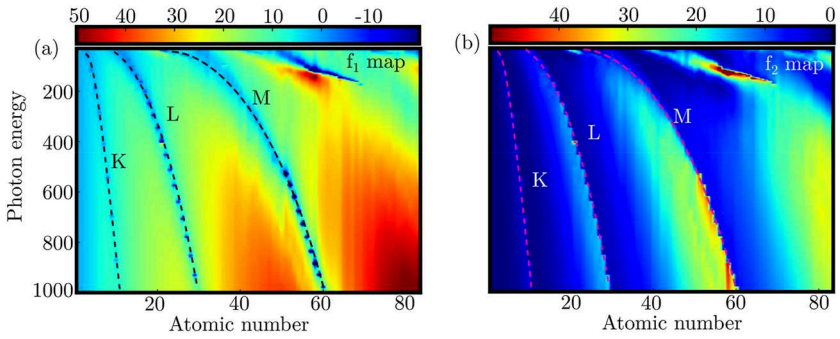

FIG. 8. (a) Map of the real part f_1 of the atomic scattering factor for all elements from 30 to 1000 eV. (b) Map of the imaginary part f_2 of the atomic scattering factor from 30 to 1000 eV. Adapted from Ref. 113.

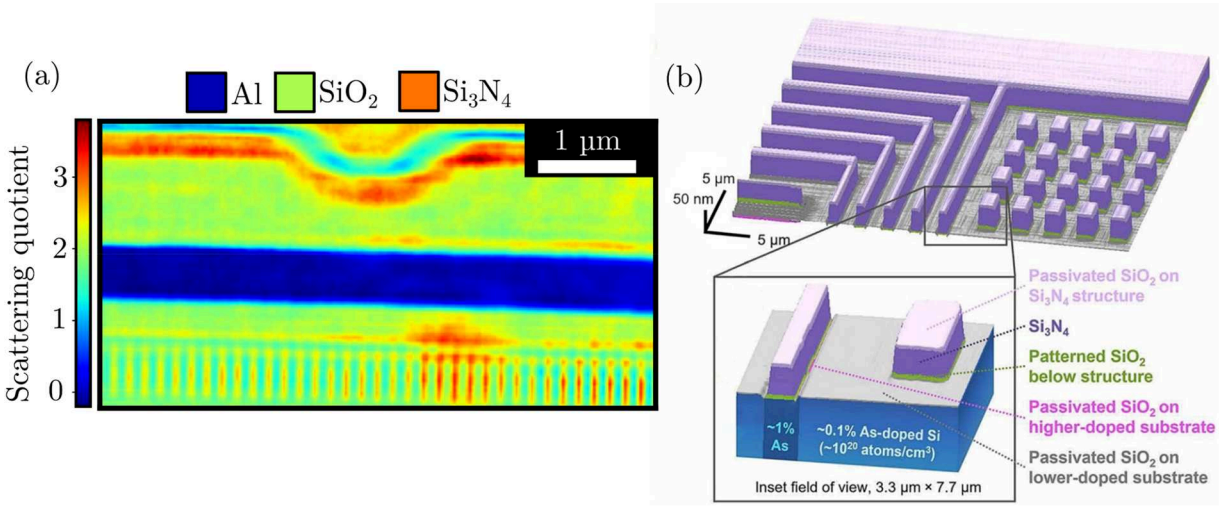

FIG. 9. (a) Scattering quotient map of an integrated circuit. The scattering quotient values of aluminum, silicon oxide, and silicon nitride are indicated. Adapted from Eschen *et al.* Light Sci Appl **11**, 117 (2022). Copyright 2022 Author(s), licensed under a Creative Commons Attribution 4.0 License. (b) Spatially and depth-resolved maps of material composition, doping, and topography. Different colors correspond to different materials. Adapted from Tanksalvala *et al.* Sci. Adv. **7**, eabd9667 (2021).[115] Copyright 2021 Author(s), licensed under a Creative Commons Attribution 4.0 License.

extracting all sample parameters from a single ptychography measurement is usually an underdetermined problem. To solve this problem, recently phase-sensitive reflectometry has been introduced employing reflection ptychography.[115,118] This approach reconstructs complex-valued objects from a set of measurements with different incident illumination angles. The resulting data allow for the calculation of reflectance curves across different regions of the sample, which vary based on material composition, topography, and other factors. To determine the depth-resolved material composition and structure, as shown in Fig. 9(b), a model-based approach can be employed, utilizing a genetic algorithm in conjunction with the Parratt formalism.[115] This method was recently applied to characterize the density of an amorphous carbon layer at a metal–diamond interface.[119]

D. HHG-driven ptychography: State-of-the-art

In recent years, a growing number of compact HHG-driven ptychography setups have emerged. In this section, these systems are compared in terms of spatial resolution (half-pitch) and throughput (resolved resolution elements per unit of time), with the performance of state-of-the-art ptychography beamlines at 3rd-generation synchrotrons. Figure 10 provides an overview, showing that the latest HHG-driven ptychography systems achieve resolutions well below 20 nm using a 13.5 nm wavelength.[71,72] In contrast, ptychography setups at synchrotron beamlines have achieved resolutions below 5 nm in the soft x-ray[7] and recently in the hard x-ray range.[9] Although HHG-driven ptychography setups typically achieve lower resolution compared to synchrotron facilities, they still provide sufficient resolution for a wide range of applications. Combined with excellent material contrast and micrometer-scale penetration depth, they reveal information that other compact microscopy methods, like visible light or electron microscopy, cannot provide. This opens up promising applications in microbiology, the semiconductor industry, and materials science.

In recent years, high-brightness HHG sources have been developed (see Fig. 1). However, the achievable HHG brightness (i.e., photon flux) is strongly dependent on the HHG wavelength. While a high brightness comparable to that of 3rd generation synchrotron facilities is achieved in the long-wavelength XUV range (~50 nm),

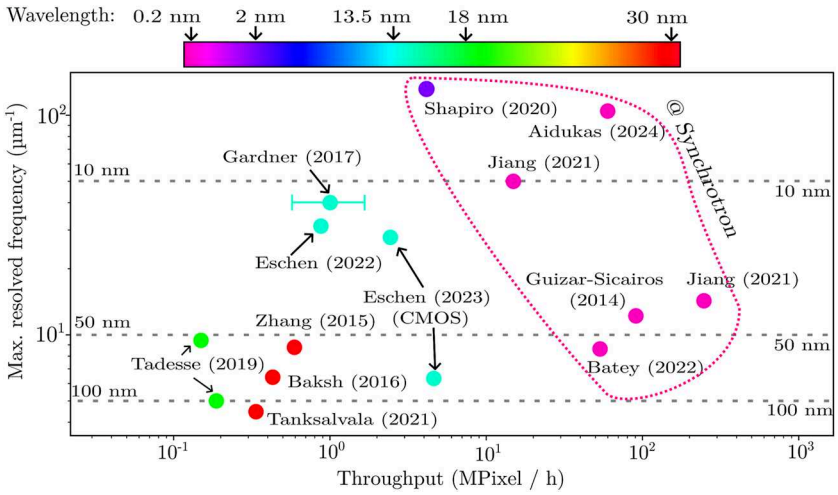

FIG. 10. Performance comparison between cutting-edge HHG-driven ptychography systems[70–72,115,120–122] and synchrotron-based ptychography setups,[7,9,123–125] focusing on half-pitch resolution and throughput. The driving wavelength is denoted by the color of each point. The required information to precisely calculate the throughput was not given in the paper for Ref. 71 and, therefore, was estimated from the given experimental parameters. Figure adapted from Ref. 113.

the brightness in the soft x-ray range (~5 nm) is significantly lower. In addition, most XUV ptychography experiments so far have relied on relatively slow CCD detectors. Recently, fast XUV sCMOS detectors have become commercially available,[126] which have enabled a throughput of up to 4.6 megapixels per hour at a wavelength of 13.5 nm,[122] with the photon flux of HHG sources at this wavelength becoming the primary limiting factor in terms of throughput. Accordingly, the throughput of HHG-driven ptychographic setups is currently about two orders of magnitude lower than that of state-of-the-art synchrotron beamlines (Fig. 10). However, at longer XUV wavelengths, such as 50 nm, coherent power in the multi-milliwatt range is available.[33] If such an HHG source is combined with the latest XUV detector generation, it is anticipated that future HHG-driven ptychography setups can achieve similar throughputs as typical imaging beamlines at present's synchrotron facilities.

It should be noted that throughput and resolution are not the sole criteria characterizing a ptychography setup. HHG-driven ptychography setups with temporal resolution,[127] multi-wavelength,[78,128] and multiplexing[129] capabilities have been developed, which are not represented by the overview given in Fig. 10.

IV. XCT: NON-DESTRUCTIVE CHEMICAL MAPPING WITH NANOSCALE AXIAL RESOLUTION

XUV and soft x-ray coherence tomography (XCT) is an imaging technique that is based on interferometry with broadband light sources.[22] Its optical counterpart is optical coherence tomography in the infrared and visible range, with its great story of success in modern ophthalmology and other medical and technical applications.[23,24]

Coherence tomography utilizes the short coherence length of broadband light sources to achieve axial resolution. In a typical generic setup realization, one mirror of a Michelson-type interferometer is replaced by a sample (sample arm of the interferometer). The light that is backscattered at different depths inside the sample is superimposed with the light of the other arm (the reference arm) of the interferometer. Both fields interfere and form a specific interference pattern at the output. Considered in the temporal domain, only the part of the backscattered light that has traveled the same optical path length as the light from the reference arm of the sample will show interference owing to the short coherence length of broadband radiation. This condition is entirely determined by the coherence length of the light source, $l_c = 2\ \ln(2)\ \lambda_0^2/\Delta\lambda$, which is fundamentally linked to the spectral bandwidth $\Delta\lambda$ and the central wavelength λ_0. Therefore, by scanning the length of the reference arm, the axial structure of the sample can be mapped with a resolution of half the coherence length. This implementation is called time-domain OCT.

Scanning the reference arm typically adds technical complexity and loss of precision. Therefore, as described by the Wiener–Khinchin-theorem,[130,131] the intensity as a function of wavelength (i.e., the spectrum) carries the same information as the intensity as a function of the length of the reference arm. This is a direct consequence of the superposition principle, which, in this case, means that interference will occur independently of the reference arm length for every wavelength individually. Therefore, the depth structure of the sample is encoded in the modulations of the

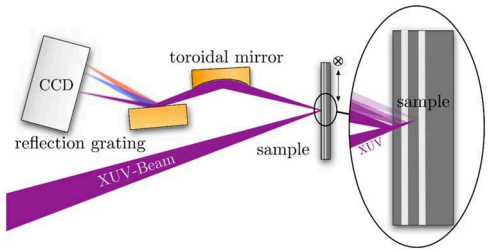

FIG. 11. Principle of XCT. A broadband XUV beam is focused on the sample. The backscattered light from different layers interferes and forms a modulated spectrum, which is measured with an XUV spectrometer. Lateral scanning of the sample enables 3D tomograms. Adapted from Fuchs *et al.* Appl. Phys. B (2012) **106**:789–795.[22] Copyright 2012 Author(s), licensed under a Creative Commons Attribution 2.0 International License.

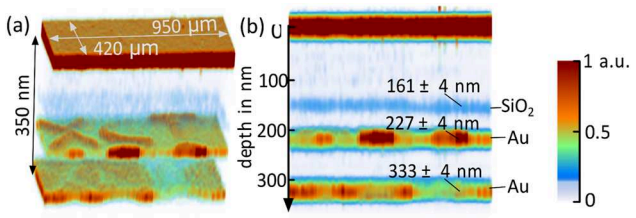

FIG. 12. 3D XCT tomogram of two laterally structured 5 nm gold layers and an additional SiO_2 layer encapsulated in silicon. The axial resolution is <24 nm, whereas the lateral resolution is <25 μm. (a) Shows an isometric view, and (b) shows the projected cross section. Adapted with permission from Fuchs *et al.*, Optica **4**, 903–906 (2017).[137] Copyright Optical Society of America.

spectrum and can be revealed by a Fourier-transform without the need to move the reference arm. This respective method is called Fourier-domain OCT and is the most common variant of OCT at present. Instead of using a broadband light source and a spectrometer, it is also possible to use a spectrally tunable source to record interference at all wavelengths consecutively, which is known as swept-source OCT.

The properties of the XUV and soft x-ray light prohibit the use of transmissive optics like beam-splitters. Therefore, the realization of a classical interferometric scheme is challenging, although not impossible.[132–136] However, most of the interferometric setups in the XUV and soft x-ray range suffer from instabilities since the requirements on vibrations scale with the wavelength, and the implementations are usually limited to a narrow spectral bandwidth—which would limit the axial resolution of XCT. Consequently, XCT is realized by utilizing a common-path interferometric Fourier-domain scheme, where the light reflected at the surface of the sample serves as the reference beam,[22] as depicted in Fig. 11.

The beams reflected at all the interfaces interfere and form spectral modulations, which are measured by a spectrometer. In addition, the absence of a distinct beam splitter, a decisive advantage of this approach, is a strongly reduced susceptibility to the detrimental effects of vibrations. The downside of the method, arising from the lack of an independent reference beam, is that the sample's axial structure cannot be reconstructed by a simple Fourier transform, since this would only provide its autocorrelation due to the missing phase information. The problem is completely equivalent to the phase retrieval problem of the above-mentioned lensless imaging methods, CDI and ptychography; however, it is reduced from two (lateral) to one (axial) dimension. As for the former, the phase information can be reconstructed by a phase retrieval algorithm and appropriate constraints. Counterintuitively, one-dimensional phase retrieval is much harder to achieve than higher dimensional problems due to missing redundancies. For XCT, a three-step phase retrieval algorithm[137] has been developed that converges robustly to the actual axial structure and, therefore, solves the problem.

Three-dimensional images can be achieved with XCT by adding lateral point-by-point scanning of the XUV focus position on the sample. Accordingly, the lateral resolution will be limited by the spot size, which is typically a few micrometers. The axial resolution,

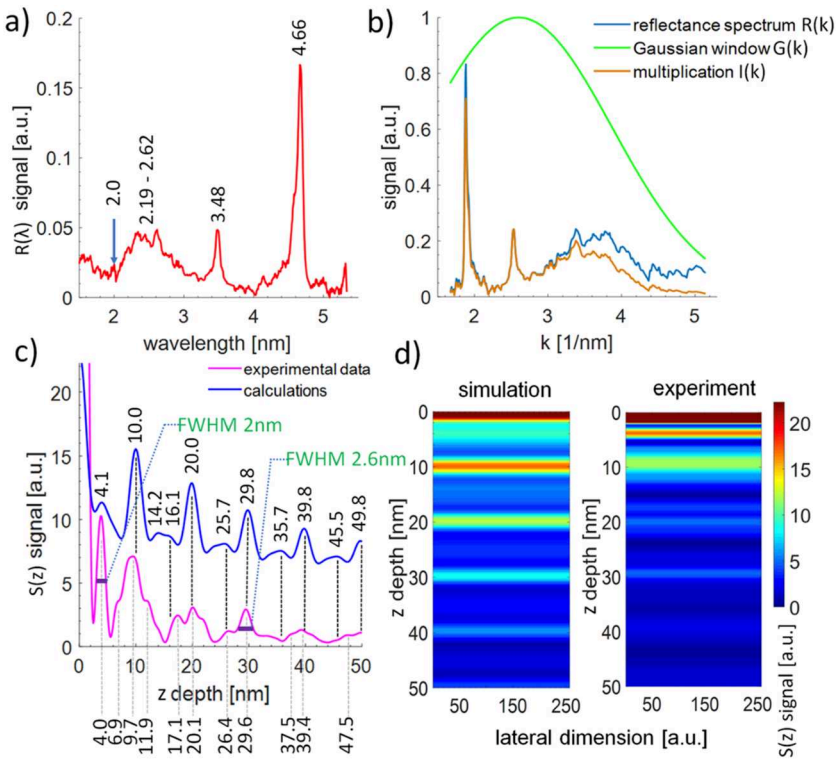

FIG. 13. (a) Measured reflectivity of a Mo/Si multilayer structure in the soft x-ray (SXR) wavelength range from 1.5 to 5.5 nm. (b) A k-space reflectivity spectrum with a Gaussian-type window applied, similar to the data presented in Fig. 1(c). (c) Reconstruction of depth information from the Mo/Si structure, with experimental data (bottom, pink curve) and simulation (top, blue curve). (d) Visualization of the sample's depth structure and a comparison between theoretical and experimental data. Recreated from Wachulak *et al.*, Sci. Rep. **8**(8494), 1–8 (2018). Copyright 2018 Author(s), licensed under a Creative Commons Attribution 4.0 License.[144]

on the other hand, remains independent of the focusing conditions and is mainly limited by the spectral properties of the light source and the sample. In the XUV, the axial resolution can reach ≈10 nm, whereas ≈2 nm is possible in the soft x-ray regime. The penetration depth depends on the absorption of the materials in the sample. By using transmission windows of a sample's dominating material, e.g., the silicon (≈30 – 100 eV) or the water window (≈2 – 4 nm), the penetration depth can reach several micrometers.

XCT has been first demonstrated at synchrotrons[138] in the silicon transmission window and in the water window. The achieved axial resolution in silicon- and boron carbide-based samples was <18 nm and <8 nm, respectively. The lateral resolution was limited to ≈100 μm by the synchrotron spot size. The axial structure reconstructed in this early work shows the autocorrelation and, therefore, exhibits artifacts, which, in later work, are mitigated by phase retrieval as mentioned earlier.

The first implementation of laboratory-scale XCT has been demonstrated using a high harmonic XUV source.[137] HHG is an intrinsically broadband source that makes it ideally suited for XCT. In fact, the majority of other HHG-based XUV imaging methods require monochromatic light and, therefore, need to discard most of the precious HHG photon flux. In contrast, XCT utilizes most of the bandwidth and, therefore, most of the generated XUV photons. However, as the name indicates, high harmonic spectra are typically strongly modulated in the spectral domain, and there are spectral gaps between the single harmonics without significant photon flux. Both would limit the applicability of XCT. To overcome this issue, an optical parametric amplifier is used to rapidly sweep the wavelength of the infrared driving laser and, therefore, the harmonics as well. Therefore, the time-averaged XUV spectrum gets sufficiently smoothed without spectral gaps in photon flux.[139]

XCT was then performed on silicon-based samples with 5 nm thin structured gold layers with a high-resolution XUV spectrometer.[140,141] The corresponding 3D XCT scan is depicted in Fig. 12 and shows a non-destructive axial resolution of <24 nm and <25 μm in the lateral dimensions. The lateral resolution was limited by the small numerical aperture of the focusing mirror, whereas the axial resolution is independent of the NA, which is a decisive advantage of the XCT method. For the first time in XCT, autocorrelation artifacts could be completely removed numerically by the above-mentioned one-dimensional phase retrieval algorithm.[137]

XCT is not limited to the spectral range of current HHG sources. The method has also been demonstrated to work with broadband plasma-based XUV sources in the silicon transmission window[142,143] as well as in the water window, leading to extraordinarily high axial resolutions down to 2 nm.[144,145] This high resolution was demonstrated by illuminating a multilayer structure with an octave-spanning spectrum within the water window, covering wavelengths from 1.5 to 5.5 nm. The corresponding results are shown in Fig. 13. Furthermore, the water window spectral range allows for even more absorption edges of different materials to be utilized for chemical mapping, especially in biological samples containing oxygen, nitrogen, and carbon.

A. Chemical and elemental mapping in XCT

The phase retrieval algorithm not only reconstructs the internal structure of the sample; rather, it also reveals the full spectral reflectivity of the sample, including the spectral phase. This broadband spectroscopic information leads to remarkably sensitive and versatile elemental and chemical contrasts in XCT. It is even possible to algorithmically reconstruct the full spectral reflectivity, including phase information from every individual layer of the sample, as has been demonstrated.[146] In Fig. 14, the reconstructed depth structure as well as the spectral reflectivities of each layer of a silicon-based sample is shown. Due to the M-edges of the materials, Si, Ti, TiO_2, and SiO_2 can clearly be distinguished. The algorithm is completely model-free and does not require any prior knowledge of the sample. However, the spectral reflectivity in amplitude and phase of each layer can then be utilized in a model-based optimization scheme to reveal additional parameters of the layers like roughness and layer thickness below the actual resolution limit of XCT without extensive sample preparation.[147]

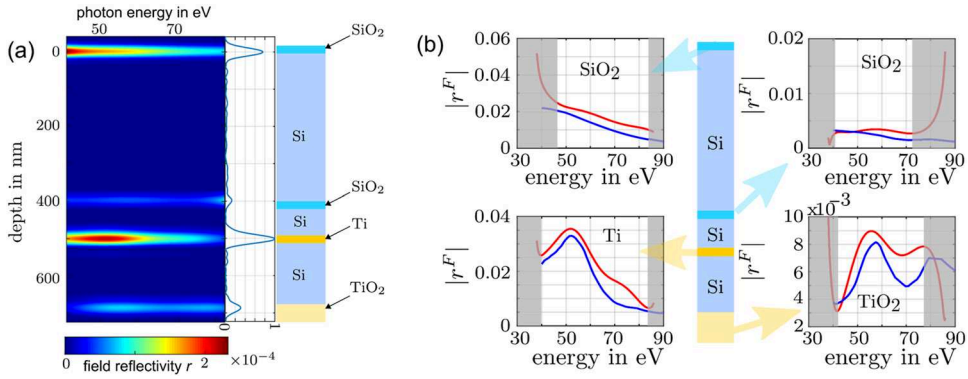

FIG. 14. XCT of a layered sample consisting of TiO_2, Ti, Si, and SiO_2 layers. (a) Shows a false color plot of the reconstructed depth structure and spectral reflectivity of all layers independently. (b) Shows the spectral reflectivity of all layers in more detail. The red curves are directly reconstructed from the measurements, whereas the blue curves are model-based simulations that were optimized, including roughness and thickness of the layers. Adapted from Wiesner *et al.* Optica **8**, 230–238 (2021).[146] Copyright 2021 Author(s), licensed under a Creative Commons Attribution 4.0 License.

B. Applications of XCT

The most distinctive properties of XCT are non-invasive and cross-sectional imaging. For some applications, this alone can be a single selling point, quite analogous to OCT for ophthalmology. Obvious study objects are, e.g., nano-devices, in particular, if they are to be investigated in-operando. Regularly, these devices will be embedded to protect them in a harsh environment. However, non-invasive and cross-sectional imagings are not the only advantages of XCT as described earlier. The elemental contrast is particularly noteworthy, especially in scenarios where it is limited in widely used techniques, such as for oxides in electron microscopy. On the one hand, this is due to XUV absorption edges characteristic for the elements. On the other hand, very high sensitivity has always been a trademark of OCT, which can be traced back to Felgett's (or the multiplex) advantage of Fourier methods. An example is the result from Ref. 137 shown in Fig. 12. Here, a ~3 nm thick SiO_2 layer, which had formed unintentionally during the production of the sample, was clearly visible. The verification of the result with an electron microscope was time-consuming, even if ignoring the fact that a thin lamella had to be cut out of the sample with a FIB apparatus.

There are several subtle aspects of the high sensitivity and non-invasive nature of XCT, which were illustrated using a sample from the field of materials science. An Al_2Cu–Al system was investigated, and XCT successfully determined all relevant properties, including layer thickness, roughness, and stoichiometric composition.[148] In particular, the buried native oxide layer between Al_2Cu and Al was detected. First, it has shown that convergence of the phase reconstruction algorithm was only possible if the existence of an oxide layer, which is notoriously hard to characterize by conventional means, is included in the phase reconstruction. In other words, failure of convergence is a clear indication of missing structures in the model; hence, phase reconstruction is a means to further increase sensitivity. Second, samples like the one discussed would be quite hard to analyze with an electron microscope, even disregarding the necessity to dissect it. The reason is that the electrons deposit a lot of energy in the sample, which can easily lead to local melting and, therefore, the destruction of the very structures under investigation.

XCT can also detect very thin layers, in particular buried layers of 2D materials such as graphene or transition-metal dichalcogenides (TMDs). In an experiment on graphene buried under 200 nm of silicon, XCT can distinguish between mono-, double-, and tri-layers simply because of different reflectivity.[147] With the model-based approach discussed earlier, additional features became accessible, particularly the roughness of the layers, but also the native SiO_2 layers that form almost inevitably during the production of the samples.

Similar measurements were performed for other 2D samples, including van der Waals heterostructures (vdW–HS). Specifically, graphene embedded in hexagonal boron nitride (hBN), MoS_2 in SiO_2, a hBN–$MoTe_2$–hBN–vdW–HS, and a $MoSe_2$–MoS_2–SiO_2–cdW–HS were imaged.[149] Due to the limited size of the TMD flakes and the thinness of the cover layers, the shape of the TMD flake pushes through the cover layer and, therefore, becomes accessible for measurement with an atomic force microscope (AFM). We find the XCT measurements in very good agreement with AFM results.

An interesting aspect concerns comparisons with simulations. These are based on the Henke database of semi-empirical scattering factors,[150] which has become a standard in XUV and x-ray physics. So far, experimental verification of this database has largely been restricted to synchrotron measurements. It shows that XCT can produce data of similar quality in the XUV spectral range. This has been convincingly demonstrated also at an Al_2O_3 substrate, where the NEXAFS feature[151] due to the $L_{2/3}$-edge was measured and directly superimposed with synchrotron measurements on the same sample as shown in Fig. 15.[152] Interestingly, the XCT measurement was much faster than the synchrotron measurement—since XCT can measure at all wavelengths at the same time. This work also demonstrates how HHG source instabilities, which typically pose a significant challenge for imaging setups, can be mitigated through a tailored *in situ* referencing scheme.

V. TRENDS AND FUTURE OPPORTUNITIES

In recent years, numerous applications of XUV ptychography and XCT, collectively referred to here as nanoscale coherent XUV

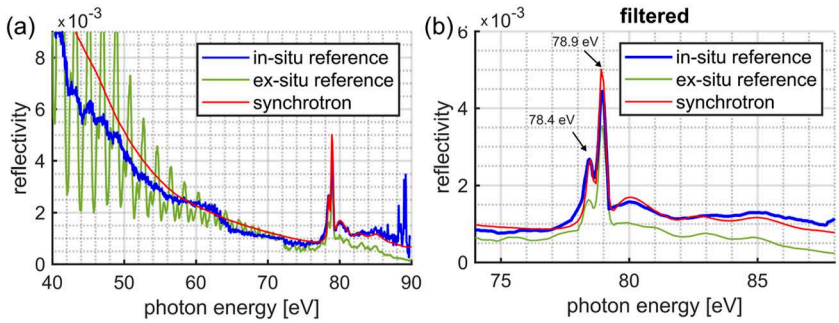

FIG. 15. (a) Measured broadband reflectivity of an Al_2O_3 sample with the laboratory XCT setup driven by high harmonic generation. Different reference schemes are compared. A new *in situ* reference leads to results that are comparable to synchrotron measurements. (b) Same reflectivity with noise filter. The two NEXAFS features of Al_2O_3 are prominent and well reproduced. Adapted from Abel *et al.*, Opt. Express **30**, 35671 (2022).[152] Copyright 2022 Author(s), licensed under a Creative Commons Attribution 4.0 License.

imaging modalities, have been reported. However, many developments and applications remain to be explored in the future. In this section, the most promising of these are discussed, and current challenges are highlighted. For this purpose, future applications are categorized into three categories: reflection imaging, transmission imaging, and wavefront sensing, which are summarized in Fig. 16.

A. Nanoscale reflection imaging

In the x-ray range, most materials exhibit low reflectivity.[150] Therefore, grazing incidence angles are typically chosen in this spectral range to allow for investigations of surfaces with a sufficient signal-to-noise ratio. In contrast, the XUV range provides sufficient reflectivity for acceptable incidence angles. For example, an incidence angle of 60° (relative to the surface normal) yields a reflectivity of R = 57% for silicon at 30 eV photon energy and s-polarization. Therefore, given the high efficiency of HHG sources in this spectral range (see Fig. 1), the XUV range is ideally suited for nanoscale imaging of surfaces and buried structures.[116] Consequently, coherent lensless imaging modalities present a promising solution for high-resolution and phase-sensitive surface metrology with high lateral and axial resolution, unlocking numerous applications in both industry and science.

However, it should be noted that the necessary tilt of the sample also results in curved diffraction patterns, leading to anisotropic sampling and resolution.[153,154] In addition, before reconstruction, the curved diffraction pattern must be interpolated onto a regular spatial frequency grid,[155] which adds additional complexity and can be prone to inaccuracies.[156,157]

1. Surface metrology

XUV radiation offers particularly good sensitivity to surface parameters such as topography, layer structure, roughness, and material composition. This is especially promising for the nondestructive and high-resolution characterization of buried structures (such as 2D materials), meta-materials,[158] and photonic circuits.[159] In fact, the first HHG-driven ptychography demonstrations were focused on reflection ptychography and already demonstrated high resolution and excellent material-specificity.[69,116]

However, ptychography offers only limited axial resolution, while XCT provides only limited lateral resolution. Therefore, combining XUV ptychography with XCT promises 3-D imaging with sub-20 nm isotropic resolution. Combining the two techniques is challenging, as XCT relies on broadband radiation, which conflicts with the coherence requirements of ptychography. In the visible spectral range, this challenge has already been addressed by using a spectrally tunable source.[160] The XUV range, however, places significantly greater demands on optical elements. For this reason, new numerical and experimental concepts for dealing with broadband diffraction data will need to be developed in the future. Initial progress has been made, demonstrating that broadband sources can, in principle, enable broadband reconstructions of the object.[78,108,161–163] However, the application of these methods to combine XUV ptychography with XCT remains to be demonstrated, and the development of further robust methods seems to be necessary.

2. Semiconductor metrology

There is an urgent need for new characterization methods for ever-smaller semiconductor devices and the critical components of advanced XUV lithography machines used in their fabrication.[164] For example, XUV ptychography is promising for the at-wavelength characterization of XUV lithography masks, where the combined amplitude and phase contrast offer advantages compared to traditional imaging modalities. In recent years, several HHG-driven ptychography setups have been realized for this kind of application.[74,165,166] However, high-resolution imaging of defects in otherwise perfectly periodic structures has rendered a major challenge for the involved ptychography algorithms.[167] Recently, it has been shown that this issue can, in principle, be solved using structured XUV beams.[104] Furthermore, current HHG sources are limited in brightness at the relevant wavelength of 13.5 nm. New HHG sources with higher brightness need to be developed for future applications. Alternatively, longer XUV wavelengths, which offer significantly higher photon flux, can also be used;[73,128] however, they do not enable at-wavelength metrology at 13.5 nm. Furthermore, the XUV and soft x-ray range is ideally suited for the metrology of advanced semiconductor devices printed on the wafer.[168] In the

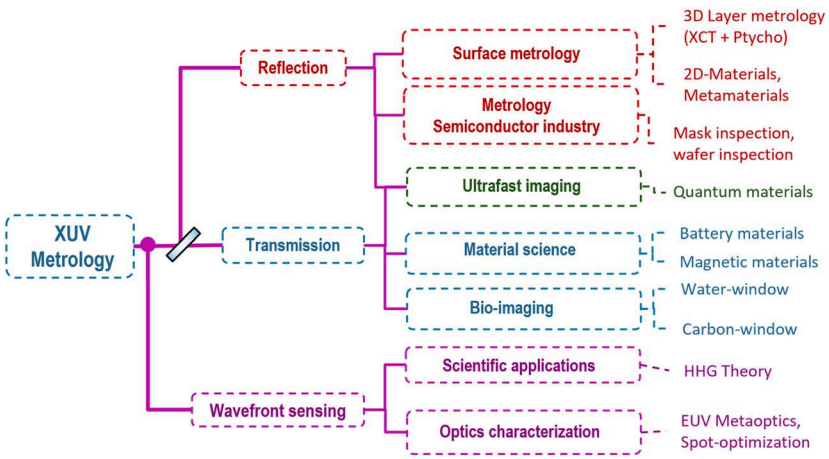

FIG. 16. Schematic illustration of future applications of coherent XUV metrology. Future applications are divided into reflection, transmission, and wavefront measurements.

future, defect sensitivity, resolution, and throughput will be key metrics that need improvement to enable industrial application. In this regard, the development of new HHG sources with higher photon fluxes will play a decisive role.

3. Ultrafast XUV imaging

An intriguing prospect for both XCT and XUV ptychography is ultrafast imaging in a pump–probe scheme. Extremely high temporal resolution is implicit in high harmonics,[169] which is so far the preferred source. Accordingly, it should become possible to image, e.g., transient magnetization or charge carrier concentration with high axial and lateral resolution. Particularly for the latter, the induced changes in scattering factors are minimal, necessitating high precision in the measurement of both phase and amplitude. However, in pioneering experiments, magnetic domains,[170] as well as thermal and acoustic dynamics,[127] were already successfully explored.

So far, the spectral reflectivity of samples is calculated with semi-empirical scattering factors, which are, however, only strictly valid for bulk material.[150] To address and understand transient phenomena, particularly in 2D materials, progress in computing XUV reflectivities is desirable. Conversely, coherent nanoscale XUV imaging can serve as an experimental testbed for progress in solid-state theory and understanding the properties of spatially heterogeneous quantum materials.[171] A key advantage of the coherent imaging modalities presented is their ability to not only extract amplitude information but also phase information of the investigated sample. It should be noted that there is a difference between XCT and XUV ptychography in time-resolved measurements. While XCT benefits from broadband XUV radiation for ptychography, a narrow bandwidth is required to achieve a high temporal coherence. This limits its applicability for extremely high temporal resolution in the attosecond range. Nevertheless, developing new ptychography methods to fully leverage a broadband continuum remains essential, with initial promising advances in lensless imaging towards imaging with attosecond temporal resolution already demonstrated.[172]

However, it should be noted that ptychography is a multi-shot technique, as multiple diffraction patterns are required for successful object reconstruction. While ptychography can, in principle, be combined with pump–probe experiments,[127] the necessary sample scanning typically results in long measurement times. In addition, non-repeatable processes cannot be studied using this approach. However, related methods are well suited for such investigations, including conventional CDI,[14,173] Fourier transform holography,[48,174–176] and coherent modulation imaging.[177,178] Furthermore, in recent years, a single-shot version of ptychography has been developed,[179–181] enabling the acquisition of a complete ptychography scan in a single exposure.

B. Nanoscale transmission imaging

Applications for transmission ptychography are predominantly determined by distinct resonances and transmission windows. Here we focus the discussion on applications in two important domains: material science and biology.

1. Material Science

Applications in the field of material science particularly benefit from the numerous elemental resonances in the XUV. For example, the M-edges of iron, nickel, and cobalt, located near 60 eV, are well suited for the investigation of magnetic order using dichroism,[182] which is important for future spintronic devices. Concurrently, state-of-the-art HHG sources provide sufficient coherent photon flux in the desired wavelength range for coherent imaging experiments.[170,183] Using HHG-driven ptychography to characterize such structures promises high-resolution imaging of extended magnetic structures with reduced requirements on the sample preparation.

In addition, important materials such as lithium and silicon offer transmission windows in the XUV that facilitate micrometer-scale penetration depths. Consequently, XUV ptychography is ideally suited for studying lithium- and silicon-based battery materials.[184] In addition, numerous other significant materials exhibit resonances in the XUV spectrum, offering promising opportunities for a wide variety of future imaging studies.

2. Bio-imaging

In recent years, high-resolution ptychography of biological specimens has been demonstrated for photon energies below 100 eV.[76,77] In these instances, wet samples are not suitable. Instead, dried samples are employed which, if properly prepared, can retain their natural structure.[185] Especially the spectral range between 130 and 170 eV (here referred to as the carbon window) appears promising, offering multiple advantages. First, carbon in this range has a relatively long absorption length in the micrometer range. Therefore, relatively thick samples can be investigated. Second, both sulfur and phosphorus offer absorption edges in the spectral range, providing good contrast for specific sub-cellular structures. Finally, established HHG sources offer sufficient photon flux and stability in this spectral range for high-resolution imaging.[32]

However, the spectral range between the carbon K-edge (~280 eV) and the oxygen K-edge (~530 eV), known as the water window, holds particular promise for imaging wet biological samples. HHG-driven ptychography of biological specimens within this range enables excellent dose efficiency, quantitative phase contrast, and high-resolution imaging, while still being accessible to a broad community due to the compact size of the involved light sources. High-resolution table-top imaging in the water window is anticipated to become feasible in the near future, driven by significant recent advancements in ultrafast IR laser development.[64,186] These advancements may soon enable high-photon-flux HHG sources in the water window, facilitating high-resolution imaging of biological samples in wet environments—a capability currently limited to plasma sources[187,188] and synchrotrons.[189,190]

C. High-resolution wavefront sensing

Ptychography also serves as an advanced, high-resolution, multi-modal wavefront sensing technique since it enables the simultaneous reconstruction of both the object and the illumination. The advantage of ptychography compared to other wavefront sensing techniques lies in its ability to reconstruct the wavefront with high resolution and, at the same time, enable the reconstruction of partially coherent[90] and multi-wavelength[91] beams. Therefore, multi-color ptychography is particularly valuable for the wavelength-resolved and high-resolution characterization of naturally broadband HHG sources. This capability is crucial for gaining comprehensive insights into the HHG process, a cornerstone for

advancements in attosecond science.[79,80] In addition, in recent years, a wide range of exotic HHG beams has been discovered.[191,192] Multi-wavelength ptychography facilitates their detailed characterization and the validation of the involved theoretical models.

Furthermore, ptychography offers a valuable tool for the characterization and optimization of optical components, including broadband diffractive optical elements[83] and, potentially, innovative high-NA XUV meta-optics,[193] which are difficult to characterize fully with other established methods.

VI. CONCLUSION

The rapid development of computational imaging methods, combined with novel high-brightness tabletop XUV sources, has, in recent years, facilitated the application of high-resolution coherent imaging modalities on a laboratory scale. Combined with advanced control of the XUV light field, this has enabled high-resolution imaging with lateral resolution down to sub-20 nm using ptychography. In contrast, using XCT high axial resolution has been achieved, allowing the characterization of single-atom layers[147,149] and, at the same time, providing information on important properties such as roughness and material composition. Therefore, XUV ptychography and XCT offer a unique combination of capabilities that complement existing imaging techniques such as electron microscopy. However, unlike electron microscopes, XUV radiation can penetrate micrometer-thick samples while providing excellent material contrast. Accordingly, it is concluded that nanoscale coherent XUV imaging is promising for the investigation of a broad range of samples ranging from microbiology to materials science. Therefore, XUV imaging holds great promise to contribute to the development of energy-efficient high-performance nanoelectronics, novel materials, and energy storage systems, all of which require innovative, high-resolution, and chemical-sensitive metrology methods. It is further anticipated that new coherent XUV sources with substantially higher brightness and photon energy will be developed in the near future, enabling the expansion of tabletop imaging experiments into the soft x-ray range and supporting industrial applications.

ACKNOWLEDGMENTS

This work was supported by the Federal State of Thuringia (Grant No. 41-5507-2016), the European Social Fund (ESF), and the Thüringer Aufbaubank (Grant Nos. 2017 FGR 0076 and 2018 FGR 0080). Additional support was provided by the European Research Council (ERC) under the European Union's Horizon 2020 research and innovation program (Grant Agreement No. 835306, SALT) and the Fraunhofer Cluster of Excellence Advanced Photon Sources. Furthermore, the research was sponsored by a Strategy and Innovation Grant from the Free State of Thuringia (Grant No. 41-5507-2016), the Innovation Pool of the Research Field Matter of the Helmholtz Association of German Research Centers (project FISCOV), and the Helmholtz Association (Grant Nos. Ptychography 4.0 and ZT-I-PF-4-018 AsoftXm). Additionally, support was provided by the Deutsche Forschungsgemeinschaft (DFG, German Research Foundation) – Project number 465215929 – Grant No. PA 730/13-1.

AUTHOR DECLARATIONS

Conflict of Interest

The authors have no conflicts to disclose.

Author Contributions

W. Eschen: Conceptualization (equal); Visualization (equal); Writing – original draft (equal); Writing – review & editing (equal). **R. Klas**: Conceptualization (equal); Visualization (equal); Writing – original draft (equal); Writing – review & editing (equal). **D.S. Penagos Molina**: Conceptualization (equal); Visualization (equal); Writing – original draft (equal); Writing – review & editing (equal). **S. Fuchs**: Conceptualization (equal); Visualization (equal); Writing – original draft (equal); Writing – review & editing (equal). **G. G. Paulus**: Conceptualization (equal); Funding acquisition (equal); Writing – original draft (equal); Writing – review & editing (equal). **J. Limpert**: Conceptualization (equal); Funding acquisition (equal); Visualization (equal); Writing – original draft (equal); Writing – review & editing (equal). **J. Rothhardt**: Conceptualization (equal); Funding acquisition (equal); Visualization (equal); Writing – original draft (equal); Writing – review & editing (equal).

DATA AVAILABILITY

Data sharing is not applicable to this article as no new data were created or analyzed in this study.

REFERENCES

[1]W. Chao, J. Kim, S. Rekawa, P. Fischer, and E. H. Anderson, "Demonstration of 12 nm resolution Fresnel zone plate lens based soft x-ray microscopy," Opt. Express **17**, 17669 (2009).

[2]J. Kirz and C. Jacobsen, "The history and future of x-ray microscopy," J. Phys. Conf. Ser. **186**(1), 012001 (2009).

[3]B. Rösner, S. Finizio, F. Koch, F. Döring, V. A. Guzenko, M. Langer, E. Kirk, B. Watts, M. Meyer, J. Loroña Ornelas, A. Späth, S. Stanescu, S. Swaraj, R. Belkhou, T. Ishikawa, T. F. Keller, B. Gross, M. Poggio, R. H. Fink, J. Raabe, A. Kleibert, and C. David, "Soft x-ray microscopy with 7 nm resolution," Optica **7**(11), 1602 (2020).

[4]J. Miao, T. Ishikawa, I. K. Robinson, and M. M. Murnane, "Beyond crystallography: Diffractive imaging using coherent x-ray light sources," Science **348**(6234), 530–535 (2015).

[5]J. Miao, D. Sayre, and H. N. Chapman, "Phase retrieval from the magnitude of the Fourier transforms of nonperiodic objects," J. Opt. Soc. Am. A **15**(6), 1662 (1998).

[6]H. N. Chapman and K. A. Nugent, "Coherent lensless x-ray imaging," Nat. Photonics **4**(12), 833–839 (2010).

[7]D. A. Shapiro, S. Babin, R. S. Celestre, W. Chao, R. P. Conley, P. Denes, B. Enders, P. Enfedaque, S. James, J. M. Joseph, H. Krishnan, S. Marchesini, K. Muriki, K. Nowrouzi, S. R. Oh, H. Padmore, T. Warwick, L. Yang, V. V. Yashchuk, Y. S. Yu, and J. Zhao, "An ultrahigh-resolution soft x-ray microscope for quantitative analysis of chemically heterogeneous nanomaterials," Sci. Adv. **6**(51), eabc4904 (2020).

[8]H. Jiang, C. Song, C.-C. Chen, R. Xu, K. S. Raines, B. P. Fahimian, C.-H. Lu, T.-K. Lee, A. Nakashima, J. Urano, T. Ishikawa, F. Tamanoi, and J. Miao, "Quantitative 3D imaging of whole, unstained cells by using x-ray diffraction microscopy," Proc. Natl. Acad. Sci. U. S. A. **107**(25), 11234–11239 (2010).

[9]T. Aidukas, N. W. Phillips, A. Diaz, E. Poghosyan, E. Müller, A. F. J. Levi, G. Aeppli, M. Guizar-Sicairos, and M. Holler, "High-performance 4-nm-resolution x-ray tomography using burst ptychography," Nature **632**(8023), 81–88 (2024).

[10]M. Ferray, A. L'Huillier, X. F. Li, L. A. Lompre, G. Mainfray, and C. Manus, "Multiple-harmonic conversion of 1064 nm radiation in rare gases," J. Phys. B: At., Mol. Opt. Phys. **21**(3), L31–L35 (1988).
[11]T. Popmintchev, M.-C. Chen, P. Arpin, M. M. Murnane, and H. C. Kapteyn, "The attosecond nonlinear optics of bright coherent x-ray generation," Nat. Photonics **4**(12), 822–832 (2010).
[12]S. Hädrich, J. Jan Rothhardt, M. Krebs, S. Demmler, A. Klenke, A. Tünnermann, and J. Limpert, "Single-pass high harmonic generation at high repetition rate and photon flux," J. Phys. B: At., Mol. Opt. Phys. **49**(17), 172002 (2016).
[13]R. A. Bartels, A. Paul, H. Green, H. C. Kapteyn, M. M. Murnane, S. Backus, I. P. Christov, Y. Liu, D. Attwood, and C. Jacobsen, "Generation of spatially coherent light at extreme ultraviolet wavelengths," Science **297**(5580), 376–378 (2002).
[14]R. L. Sandberg, A. Paul, D. A. Raymondson, S. Hädrich, D. M. Gaudiosi, J. Holtsnider, R. I. Tobey, O. Cohen, M. M. Murnane, H. C. Kapteyn, C. Song, J. Miao, Y. Liu, and F. Salmassi, "Lensless diffractive imaging using tabletop coherent high-harmonic soft-x-ray beams," Phys. Rev. Lett. **99**(9), 098103 (2007).
[15]P. Thibault, M. Dierolf, O. Bunk, A. Menzel, and F. Pfeiffer, "Probe retrieval in ptychographic coherent diffractive imaging," Ultramicroscopy **109**(4), 338–343 (2009).
[16]P. Thibault, M. Dierolf, A. Menzel, O. Bunk, C. David, and F. Pfeiffer, "High-resolution scanning x-ray diffraction microscopy," Science **321**(5887), 379–382 (2008).
[17]A. M. Maiden and J. M. Rodenburg, "An improved ptychographical phase retrieval algorithm for diffractive imaging," Ultramicroscopy **109**(10), 1256–1262 (2009).
[18]M. Guizar-Sicairos and J. R. Fienup, "Phase retrieval with transverse translation diversity: A nonlinear optimization approach," Opt. Express **16**(10), 7264 (2008).
[19]J. R. Fienup, "Phase retrieval algorithms: A comparison," Appl. Opt. **21**(15), 2758 (1982).
[20]J. Rothhardt, G. K. Tadesse, W. Eschen, and J. Limpert, "Table-top nanoscale coherent imaging with XUV light," J. Opt. **20**(11), 113001 (2018).
[21]L. Loetgering, S. Witte, and J. Rothhardt, "Advances in laboratory-scale ptychography using high harmonic sources [Invited]," Opt. Express **30**(3), 4133 (2022).
[22]S. Fuchs, A. Blinne, C. Rödel, U. Zastrau, V. Hilbert, M. Wünsche, J. Bierbach, E. Frumker, E. Förster, and G. G. Paulus, "Optical coherence tomography using broad-bandwidth XUV and soft x-ray radiation," Appl. Phys. B **106**(4), 789–795 (2012).
[23]D. Huang, E. A. Swanson, C. P. Lin, J. S. Schuman, W. G. Stinson, W. Chang, M. R. Hee, T. Flotte, K. Gregory, C. A. Puliafito, and J. G. Fujimoto, "Optical coherence tomography," Science **254**(5035), 1178–1181 (1991).
[24]W. Drexler and J. G. Fujimoto, *Optical Coherence Tomography: Technology and Applications*, 2nd ed. (Springer International Publishing, 2015), pp. 1–2571.
[25]C. Jacobsen, *X-Ray Microscopy* (Cambridge University Press, 2019).
[26]Typically, the average brightness is expressed in photons/s/mm^2/mrad^2/0.1% BW. In the HHG community, coherent power is commonly used instead of brightness since a laser beam is naturally close to being diffraction limited. The coherent power P_{coh} at wavelength λ for a given spectral width is given by Ref. 38: $P_{coh}^{avg} = B_s^{avg} \cdot \lambda^2$. It should be noted that the spatial extent of HHG sources due to aberrations is usually not characterized. For the calculated brightness values presented here, a spatial beam quality value of $M^2 = 1.5$ is assumed.
[27]See https://www.wayforlight.eu/facility/21292 for more information about BESSY II Synchrotron.
[28]See https://als.lbl.gov/machine-information/ for more information about ALS Synchrotron.
[29]See https://indico.cern.ch/event/566138/contributions/2287596/attachments/1392404/2158746/roque-infieri-2017.pdf for more information about LNLS Sirius SynchrotronLNLS Sirius Synchrotron.
[30]See https://photon-science.desy.de/research/students__teaching/sr_and_fel_basics/fel_basics/tdr_spectral_characteristics/index_eng.html for more information about DESY FEL.
[31]S. Hädrich, A. Klenke, J. Rothhardt, M. Krebs, A. Hoffmann, O. Pronin, V. Pervak, J. Limpert, and A. Tünnermann, "High photon flux table-top coherent extreme-ultraviolet source," Nat. Photonics **8**(10), 779–783 (2014).
[32]R. Klas, W. Eschen, A. Kirsche, J. Rothhardt, and J. Limpert, "Generation of coherent broadband high photon flux continua in the XUV with a sub-two-cycle fiber laser," Opt. Express **28**(5), 6188 (2020).
[33]R. Klas, A. Kirsche, M. Gebhardt, J. Buldt, H. Stark, S. Hädrich, J. Rothhardt, and J. Limpert, "Ultra-short-pulse high-average-power megahertz-repetition-rate coherent extreme-ultraviolet light source," PhotoniX **2**(1), 4 (2021).
[34]M. Tschernajew, S. Hädrich, R. Klas, M. Gebhardt, R. Horsten, S. Weerdenburg, S. Pyatchenkov, W. Coene, J. Rothhardt, T. Eidam, and J. Limpert, "High repetition rate high harmonic generation with ultra-high photon flux," in *Laser Congress 2020 (ASSL, LAC)* (Optica Publishing Group, Washington, D.C., 2020), p. JTh2A.21.
[35]A. Comby, D. Descamps, S. Beauvarlet, A. Gonzalez, F. Guichard, S. Petit, Y. Zaouter, and Y. Mairesse, "Cascaded harmonic generation from a fiber laser: A milliwatt XUV source," Opt. Express **27**(15), 20383 (2019).
[36]G. Fan, K. Légaré, V. Cardin, X. Xie, R. Safaei, E. Kaksis, G. Andriukaitis, A. Pugžlys, B. E. Schmidt, J. P. Wolf, M. Hehn, G. Malinowski, B. Vodungbo, E. Jal, J. Lüning, N. Jaouen, G. Giovannetti, F. Calegari, Z. Tao, A. Baltuška, F. Légaré, and T. Balčiūnas, "Ultrafast magnetic scattering on ferrimagnets enabled by a bright Yb-based soft x-ray source," Optica **9**(4), 399 (2022).
[37]G. Porat, C. M. Heyl, S. B. Schoun, C. Benko, N. Dörre, K. L. Corwin, and J. Ye, "Phase-matched extreme-ultraviolet frequency-comb generation," Nat. Photonics **12**(7), 387–391 (2018).
[38]D. Popmintchev, B. R. Galloway, M. C. Chen, F. Dollar, C. A. Mancuso, A. Hankla, L. Miaja-Avila, G. O'Neil, J. M. Shaw, G. Fan, S. Ališauskas, G. Andriukaitis, T. Balčiunas, O. D. Mücke, A. Pugzlys, A. Baltuška, H. C. Kapteyn, T. Popmintchev, and M. M. Murnane, "Near- and extended-edge x-ray-absorption fine-structure spectroscopy using ultrafast coherent high-order harmonic supercontinua," Phys. Rev. Lett. **120**(9), 093002 (2018).
[39]D. Popmintchev, C. Hernández-García, F. Dollar, C. Mancuso, J. A. Pérez-Hernández, M.-C. Chen, A. Hankla, X. Gao, B. Shim, A. L. Gaeta, M. Tarazkar, D. A. Romanov, R. J. Levis, J. A. Gaffney, M. Foord, S. B. Libby, A. Jaron-Becker, A. Becker, L. Plaja, M. M. Murnane, H. C. Kapteyn, and T. Popmintchev, "Ultraviolet surprise: Efficient soft x-ray high-harmonic generation in multiply ionized plasmas," Science **350**(6265), 1225 (2015).
[40]A. Kirsche, M. Gebhardt, R. Klas, L. Eisenbach, W. Eschen, J. Buldt, H. Stark, J. Rothhardt, and J. Limpert, "Continuously tunable high photon flux high harmonic source," Opt. Express **31**(2), 2744 (2023).
[41]M. van Mörbeck-Bock, T. Feng, A. Heilmann, L. Ehrentraut, H. Stiel, M. Hennecke, T. Sidiropoulos, C. von Korff Schmising, S. Eisebitt, and M. Schnuerer, "High average power OPCPA MIR-systems for coherent soft x-ray generation accessing inner-shell absorption edges of metals," Proc. SPIE **11777**, 11777C (2021).
[42]D. H. Martz, M. Selin, O. von Hofsten, E. Fogelqvist, A. Holmberg, U. Vogt, H. Legall, G. Blobel, C. Seim, H. Stiel, and H. M. Hertz, "High average brightness water window source for short-exposure cryomicroscopy," Opt. Lett. **37**(21), 4425 (2012).
[43]P. Mayer, D. C. Brandt, I. Fomenkov, M. Purvis, and D. Brown, "Laser produced plasma EUV sources for N5 HVM and beyond: Performance, availability and technology innovation," Proc. SPIE **11609**, 1160918 (2021).
[44]T. Mey, M. Rein, P. Großmann, and K. Mann, "Brilliance improvement of laser-produced soft x-ray plasma by a barrel shock," New J. Phys. **14**(7), 073045 (2012).
[45]C. D. Macchietto, B. R. Benware, and J. J. Rocca, "Generation of millijoule-level soft-x-ray laser pulses at a 4-Hz repetition rate in a highly saturated tabletop capillary discharge amplifier," Opt. Lett. **24**(16), 1115 (1999).
[46]A. Depresseux, E. Oliva, J. Gautier, F. Tissandier, J. Nejdl, M. Kozlova, G. Maynard, J. P. Goddet, A. Tafzi, A. Lifschitz, H. T. Kim, S. Jacquemot, V. Malka, K. Ta Phuoc, C. Thaury, P. Rousseau, G. Iaquaniello, T. Lefrou, A. Flacco, B. Vodungbo, G. Lambert, A. Rousse, P. Zeitoun, and S. Sebban, "Table-top femtosecond soft x-ray laser by collisional ionization gating," Nat. Photonics **9**(12), 817–821 (2015).
[47]J. Miao, P. Charalambous, J. Kirz, and D. Sayre, "Extending the methodology of x-ray crystallography to allow imaging of micrometre-sized non-crystalline specimens," Nature **400**(6742), 342–344 (1999).
[48]S. Eisebitt, J. Lüning, W. F. Schlotter, M. Lörgen, O. Hellwig, W. Eberhardt, and J. Stöhr, "Lensless imaging of magnetic nanostructures by x-ray spectro-holography," Nature **432**(7019), 885–888 (2004).

[49]H. N. Chapman, "Phase-retrieval x-ray microscopy by Wigner-distribution deconvolution," Ultramicroscopy **66**(3–4), 153–172 (1996).
[50]D. H. Bilderback, P. Elleaume, and E. Weckert, "Review of third and next generation synchrotron light sources," J. Phys. B: At., Mol. Opt. Phys. **38**(9), S773–S797 (2005).
[51]H. N. Chapman, "Fourth-generation light sources," IUCrJ **10**(3), 246–247 (2023).
[52]E. A. Seddon, J. A. Clarke, D. J. Dunning, C. Masciovecchio, C. J. Milne, F. Parmigiani, D. Rugg, J. C. H. Spence, N. R. Thompson, K. Ueda, S. M. Vinko, J. S. Wark, and W. Wurth, "Short-wavelength free-electron laser sources and science: A review," Rep. Prog. Phys. **80**(11), 115901 (2017).
[53]H. N. Chapman, A. Barty, M. J. Bogan, S. Boutet, M. Frank, S. P. Hau-Riege, S. Marchesini, B. W. Woods, S. Bajt, W. H. Benner, R. A. London, E. Plönjes, M. Kuhlmann, R. Treusch, S. Düsterer, T. Tschentscher, J. R. Schneider, E. Spiller, T. Möller, C. Bostedt, M. Hoener, D. A. Shapiro, K. O. Hodgson, D. van der Spoel, F. Burmeister, M. Bergh, C. Caleman, G. Huldt, M. M. Seibert, F. R. N. C. Maia, R. W. Lee, A. Szöke, N. Timneanu, and J. Hajdu, "Femtosecond diffractive imaging with a soft-x-ray free-electron laser," Nat. Phys. **2**(12), 839–843 (2006).
[54]O. O. Versolato, J. Sheil, S. Witte, W. Ubachs, and R. Hoekstra, "Microdroplet-tin plasma sources of EUV radiation driven by solid-state-lasers (Topical Review)," J. Opt. **24**(5), 054014 (2022).
[55]J. J. Rocca, "Table-top soft x-ray lasers," Rev. Sci. Instrum. **70**(10), 3799–3827 (1999).
[56]V. Hilbert, M. Tschernajew, R. Klas, J. Limpert, and J. Rothhardt, "A compact, turnkey, narrow-bandwidth, tunable, and high-photon-flux extreme ultraviolet source," AIP Adv. **10**(4), 45227 (2020).
[57]K. Bergmann, "Extreme ultraviolet radiation sources from dense plasmas," Atoms **11**(9), 118 (2023).
[58]O. O. Versolato, "Physics of laser-driven tin plasma sources of EUV radiation for nanolithography," Plasma Sources Sci. Technol. **28**(8), 083001 (2019).
[59]R. Weissenbilder, S. Carlström, L. Rego, C. Guo, C. M. Heyl, P. Smorenburg, E. Constant, C. L. Arnold, and A. L'Huillier, "How to optimize high-order harmonic generation in gases," Nat. Rev. Phys. **4**(11), 713–722 (2022).
[60]P. B. Corkum, "Plasma perspective on strong field multiphoton ionization," Phys. Rev. Lett. **71**(13), 1994 (1993).
[61]T. Gaumnitz, A. Jain, Y. Pertot, M. Huppert, I. Jordan, F. Ardana-Lamas, and H. J. Wörner, "Streaking of 43-attosecond soft-x-ray pulses generated by a passively CEP-stable mid-infrared driver," Opt. Express **25**(22), 27506 (2017).
[62]C. Grebing, M. Müller, J. Buldt, H. Stark, and J. Limpert, "Kilowatt-average-power compression of millijoule pulses in a gas-filled multi-pass cell," Opt. Lett. **45**(22), 6250 (2020).
[63]M. Karst, P. Pfaller, R. Klas, Z. Wang, P. Gierschke, J. Rothhardt, and J. Limpert, "22-W average power high pulse energy multipass-cell-based post-compression in the green spectral range," Opt. Lett. **48**(5), 1300 (2023).
[64]Z. Wang, T. Heuermann, M. Gebhardt, M. Lenski, P. Gierschke, R. Klas, J. Rothhardt, C. Jauregui, and J. Limpert, "Nonlinear pulse compression to sub-two-cycle, 1.3 mJ pulses at 1.9 μm wavelength with 132 W average power," Opt. Lett. **48**(10), 2647 (2023).
[65]G. Vaschenko, C. Brewer, F. Brizuela, Y. Wang, M. A. Larotonda, B. M. Luther, M. C. Marconi, J. J. Rocca, C. S. Menoni, E. H. Anderson, W. Chao, B. D. Harteneck, J. A. Liddle, Y. Liu, and D. T. Attwood, "Sub-38 nm resolution tabletop microscopy with 13 nm wavelength laser light," Opt. Lett. **31**(9), 1214–1216 (2006).
[66]E. B. Malm, N. C. Monserud, C. G. Brown, P. W. Wachulak, H. Xu, G. Balakrishnan, W. Chao, E. Anderson, and M. C. Marconi, "Tabletop single-shot extreme ultraviolet Fourier transform holography of an extended object," Opt. Express **21**(8), 9959 (2013).
[67]W. Hoppe, "Beugung im inhomogenen Primärstrahlwellenfeld. I. Prinzip einer Phasenmessung von Elektronenbeungungsinterferenzen," Acta Crystallogr., Sect. A **25**(4), 495–501 (1969).
[68]F. Pfeiffer, "X-ray ptychography," Nat. Photonics **12**(1), 9–17 (2018).
[69]M. D. Seaberg, B. Zhang, D. F. Gardner, E. R. Shanblatt, M. M. Murnane, H. C. Kapteyn, and D. E. Adams, "Tabletop nanometer extreme ultraviolet imaging in an extended reflection mode using coherent Fresnel ptychography," Optica **1**(1), 39 (2014).
[70]P. D. Baksh, M. Odstrčil, H.-S. Kim, S. A. Boden, J. G. Frey, and W. S. Brocklesby, "Wide-field broadband extreme ultraviolet transmission ptychography using a high-harmonic source," Opt. Lett. **41**(7), 1317 (2016).
[71]D. F. Gardner, M. Tanksalvala, E. R. Shanblatt, X. Zhang, B. R. Galloway, C. L. Porter, R. Karl, Jr., C. Bevis, D. E. Adams, H. C. Kapteyn, M. M. Murnane, and G. F. Mancini, "Subwavelength coherent imaging of periodic samples using a 13.5 nm tabletop high-harmonic light source," Nat. Photonics **11**(4), 259–263 (2017).
[72]W. Eschen, L. Loetgering, V. Schuster, R. Klas, A. Kirsche, L. Berthold, M. Steinert, T. Pertsch, H. Gross, M. Krause, J. Limpert, and J. Rothhardt, "Material-specific high-resolution table-top extreme ultraviolet microscopy," Light Sci. Appl. **11**(1), 117 (2022).
[73]H. Lu, M. Odstrčil, C. Pooley, J. Biller, M. Mebonia, G. He, M. Praeger, L. Juschkin, J. Frey, and W. Brocklesby, "Characterisation of engineered defects in extreme ultraviolet mirror substrates using lab-scale extreme ultraviolet reflection ptychography," Ultramicroscopy **249**, 113720 (2023).
[74]B. Wang, N. Brooks, M. Tanksalvala, Y. Esashi, N. Jenkins, P. Johnsen, I. Binnie, G. Gui, Y. Shao, M. Murnane, and H. Kapteyn, "Robust and reliable actinic ptychographic imaging of highly periodic structures in EUV photomasks," Proc. SPIE **12293**, 122930D (2022).
[75]D. G. Lee, Y. W. Kim, S. Moon, and J. Ahn, "Effect of wrinkles on extreme ultraviolet pellicle reflectivity and local critical dimension," Appl. Opt. **61**(20), 5965 (2022).
[76]P. D. Baksh, M. Ostrčil, M. Miszczak, C. Pooley, R. T. Chapman, A. S. Wyatt, E. Springate, J. E. Chad, K. Deinhardt, J. G. Frey, and W. S. Brocklesby, "Quantitative and correlative extreme ultraviolet coherent imaging of mouse hippocampal neurons at high resolution," Sci. Adv. **6**(18), eaaz3025 (2020).
[77]C. Liu, W. Eschen, L. Loetgering, D. S. Penagos Molina, R. Klas, A. Iliou, M. Steinert, S. Herkersdorf, A. Kirsche, T. Pertsch, F. Hillmann, J. Limpert, and J. Rothhardt, "Visualizing the ultra-structure of microorganisms using table-top extreme ultraviolet imaging," PhotoniX **4**(1), 6 (2023).
[78]B. Zhang, D. F. Gardner, M. H. Seaberg, E. R. Shanblatt, C. L. Porter, R. Karl, C. A. Mancuso, H. C. Kapteyn, M. M. Murnane, and D. E. Adams, "Ptychographic hyperspectral spectromicroscopy with an extreme ultraviolet high harmonic comb," Opt. Express **24**(16), 18745 (2016).
[79]X. Liu, A. Pelekanidis, M. Du, F. Zhang, K. S. E. Eikema, and S. Witte, "Observation of chromatic effects in high-order harmonic generation," Phys. Rev. Res. **5**(4), 043100 (2023).
[80]M. Du, X. Liu, A. Pelekanidis, F. Zhang, L. Loetgering, P. Konold, C. L. Porter, P. Smorenburg, K. S. E. Eikema, and S. Witte, "High-resolution wavefront sensing and aberration analysis of multi-spectral extreme ultraviolet beams," Optica **10**(2), 255–263 (2023).
[81]D. Goldberger, D. Schmidt, J. Barolak, B. Ivanic, C. G. Durfee, and D. E. Adams, "Spatiospectral characterization of ultrafast pulse-beams by multiplexed broadband ptychography," Opt. Express **29**(20), 32474 (2021).
[82]A. Pelekanidis, F. Zhang, K. S. E. Eikema, and S. Witte, "Generation dynamics of broadband extreme ultraviolet vortex beams," ACS Photonics **12**, 1638 (2025).
[83]L. Loetgering, X. Liu, A. C. C. De Beurs, M. Du, G. Kuijper, K. S. E. Eikema, and S. Witte, "Tailoring spatial entropy in extreme ultraviolet focused beams for multispectral ptychography," Optica **8**(2), 130 (2021).
[84]O. Pronin, V. Pervak, E. Fill, J. Rauschenberger, F. Krausz, and A. Apolonski, "Ultrabroadband efficient intracavity XUV output coupler," Opt. Express **19**(11), 10232 (2011).
[85]M. Odstrcil, P. Baksh, S. A. Boden, R. Card, J. E. Chad, J. G. Frey, and W. S. Brocklesby, "Ptychographic coherent diffractive imaging with orthogonal probe relaxation," Opt. Express **24**(8), 8360 (2016).
[86]F. Zhang, I. Peterson, J. Vila-Comamala, A. Diaz, F. Berenguer, R. Bean, B. Chen, A. Menzel, I. K. Robinson, and J. M. Rodenburg, "Translation position determination in ptychographic coherent diffraction imaging," Opt. Express **21**(11), 13592 (2013).
[87]O. Bunk, M. Dierolf, S. Kynde, I. Johnson, O. Marti, and F. Pfeiffer, "Influence of the overlap parameter on the convergence of the ptychographical iterative engine," Ultramicroscopy **108**(5), 481–487 (2008).
[88]E. H. R. Tsai, I. Usov, A. Diaz, A. Menzel, and M. Guizar-Sicairos, "X-ray ptychography with extended depth of field," Opt. Express **24**(25), 29089 (2016).
[89]F. van der Veen, F. Pfeiffer, F. Van Der Veen, and F. Pfeiffer, "Coherent x-ray scattering," J. Phys.: Condens. Matter **16**(28), 5003–5030 (2004).

[90]P. Thibault and A. Menzel, "Reconstructing state mixtures from diffraction measurements," Nature **494**(7435), 68–71 (2013).
[91]D. J. Batey, D. Claus, and J. M. Rodenburg, "Information multiplexing in ptychography," Ultramicroscopy **138**, 13–21 (2014).
[92]A. M. Maiden, M. J. Humphry, and J. M. Rodenburg, "Ptychographic transmission microscopy in three dimensions using a multi-slice approach," J. Opt. Soc. Am. A **29**(8), 1606 (2012).
[93]B. Enders and P. Thibault, "A computational framework for ptychographic reconstructions," Proc. R. Soc. A **472**(2196), 20160640 (2016).
[94]K. Wakonig, H.-C. Stadler, M. Odstrčil, E. H. R. Tsai, A. Diaz, M. Holler, I. Usov, J. Raabe, A. Menzel, and M. Guizar-Sicairos, "PtychoShelves, a versatile high-level framework for high-performance analysis of ptychographic data," J. Appl. Crystallogr. **53**(2), 574–586 (2020).
[95]L. Loetgering, M. Du, D. Boonzajer Flaes, T. Aidukas, F. Wechsler, D. S. Penagos Molina, M. Rose, A. Pelekanidis, W. Eschen, J. Hess, T. Wilhein, R. Heintzmann, J. Rothhardt, and S. Witte, "PtyLab.m/py/jl: A cross-platform, open-source inverse modeling toolbox for conventional and fourier ptychography," Opt. Express **31**(9), 13763 (2023).
[96]J. Rodenburg and A. Maiden, *Ptychography* (Springer International Publishing, Cham, 2019).
[97]A. L'Huillier, P. Balcou, S. Candel, K. J. Schafer, and K. C. Kulander, "Calculations of high-order harmonic-generation processes in xenon at 1064 nm," Phys. Rev. A **46**(5), 2778–2790 (1992).
[98]B. Enders, "Development and application of decoherence models in ptychographic diffraction imaging," Ph.D.thesis, Technische Universität München, 2016.
[99]M. Guizar-Sicairos, M. Holler, A. Diaz, J. Vila-Comamala, O. Bunk, and A. Menzel, "Role of the illumination spatial-frequency spectrum for ptychography," Phys. Rev. B **86**(10), 100103 (2012).
[100]M. Odstrčil, M. Lebugle, M. Guizar-Sicairos, C. David, and M. Holler, "Towards optimized illumination for high-resolution ptychography," Opt. Express **27**(10), 14981–14997 (2019).
[101]A. M. Maiden, G. R. Morrison, B. Kaulich, A. Gianoncelli, and J. M. Rodenburg, "Soft x-ray spectromicroscopy using ptychography with randomly phased illumination," Nat. Commun. **4**(1), 1669 (2013).
[102]S. Marchesini and A. Sakdinawat, "Shaping coherent x-rays with binary optics," Opt. Express **27**(2), 907 (2019).
[103]W. Eschen, C. Liu, M. Steinert, D. S. Penagos Molina, T. Siefke, U. D. Zeitner, J. Kaspar, T. Pertsch, J. Limpert, and J. Rothhardt, "Structured illumination ptychography and at-wavelength characterization with an EUV diffuser at 13.5 nm wavelength," Opt. Express **32**(3), 3480 (2024).
[104]B. Wang, N. J. Brooks, P. Johnsen, N. W. Jenkins, Y. Esashi, I. Binnie, M. Tanksalvala, H. C. Kapteyn, and M. M. Murnane, "High-fidelity ptychographic imaging of highly periodic structures enabled by vortex high harmonic beams," Optica **10**(9), 1245 (2023).
[105]M. Zürch, C. Kern, P. Hansinger, A. Dreischuh, and Ch. Spielmann, "Strong-field physics with singular light beams," Nat. Phys. **8**(10), 743–746 (2012).
[106]C. Hernández-García, A. Picón, J. San Román, and L. Plaja, "Attosecond extreme ultraviolet vortices from high-order harmonic generation," Phys. Rev. Lett. **111**(8), 083602 (2013).
[107]G. S. M. Jansen, D. Rudolf, L. Freisem, K. S. E. Eikema, and S. Witte, "Spatially resolved Fourier transform spectroscopy in the extreme ultraviolet," Optica **3**(10), 1122 (2016).
[108]J. Huijts, S. Fernandez, D. Gauthier, M. Kholodtsova, A. Maghraoui, K. Medjoubi, A. Somogyi, W. Boutu, and H. Merdji, "Broadband coherent diffractive imaging," Nat. Photonics **14**, 618 (2020).
[109]R. A. Dilanian, B. Chen, G. J. Williams, H. M. Quiney, K. A. Nugent, S. Teichmann, P. Hannaford, L. V. Dao, and A. G. Peele, "Diffractive imaging using a polychromatic high-harmonic generation soft-x-ray source," J. Appl. Phys. **106**(2), 23110 (2009).
[110]C. Chen, H. Gu, and S. Liu, "Ultra-broadband diffractive imaging with unknown probe spectrum," Light Sci. Appl. **13**(1), 213 (2024).
[111]B. Shearer, H. Kapteyn, I. Binnie, N. W. Jenkins, and M. Murnane, "Robust broadband ptychography algorithms for high-harmonic soft x-ray supercontinua," Opt. Express **33**(1), 717 (2025).
[112]A. Rana, J. Zhang, M. Pham, A. Yuan, Y. H. Lo, H. Jiang, S. Osher, and J. Miao, "Potential of attosecond coherent diffractive imaging," Phys. Rev. Lett. **125**, 086101 (2020).
[113]W. Eschen, "Material-specific and high-resolution imaging using extreme ultraviolet ptychography," Ph.D. dissertation (Friedrich-Schiller-Universität Jena, 2024).
[114]M. W. M. Jones, K. Elgass, M. D. Junker, M. B. Luu, M. T. Ryan, A. G. Peele, and G. A. Van Riessen, "Mapping biological composition through quantitative phase and absorption x-ray ptychography," Sci. Rep. **4**(1), 6796 (2014).
[115]M. Tanksalvala, C. L. Porter, Y. Esashi, B. Wang, N. W. Jenkins, Z. Zhang, G. P. Miley, J. L. Knobloch, B. McBennett, N. Horiguchi, S. Yazdi, J. Zhou, M. N. Jacobs, C. S. Bevis, R. M. Karl, P. Johnsen, D. Ren, L. Waller, D. E. Adams, S. L. Cousin, C. T. Liao, J. Miao, M. Gerrity, H. C. Kapteyn, and M. M. Murnane, "Nondestructive, high-resolution, chemically specific 3D nanostructure characterization using phase-sensitive EUV imaging reflectometry," Sci. Adv. **7**(5), 9667–9694 (2021).
[116]E. R. Shanblatt, C. L. Porter, D. F. Gardner, G. F. Mancini, R. M. Karl, M. D. Tanksalvala, C. S. Bevis, V. H. Vartanian, H. C. Kapteyn, D. E. Adams, and M. M. Murnane, "Quantitative chemically specific coherent diffractive imaging of reactions at buried interfaces with few nanometer precision," Nano Lett. **16**(9), 5444–5450 (2016).
[117]Y. Shao, S. Weerdenburg, J. Seifert, H. P. Urbach, A. P. Mosk, and W. Coene, "Wavelength-multiplexed multi-mode EUV reflection ptychography based on automatic differentiation," Light Sci. Appl. **13**(1), 196 (2024).
[118]Y. Esashi, N. W. Jenkins, Y. Shao, J. M. Shaw, S. Park, M. M. Murnane, H. C. Kapteyn, and M. Tanksalvala, "Tabletop extreme ultraviolet reflectometer for quantitative nanoscale reflectometry, scatterometry, and imaging," Rev. Sci. Instrum. **94**(12), 123705 (2023).
[119]B. McBennett, Y. Esashi, N. W. Jenkins, A. Beardo, Y. Shao, E. E. Nelson, T. H. Culman, B. Abad, M. Tanksalvala, T. D. Frazer, S. Marks, W. Chao, S. Yazdi, J. L. Knobloch, H. C. Kapteyn, and M. M. Murnane, "Low-density diamondlike amorphous carbon at nanostructured metal-diamond interfaces," Phys. Rev. Mater. **8**(9), 096001 (2024).
[120]G. K. Tadesse, W. Eschen, R. Klas, M. Tschernajew, F. Tuitje, M. Steinert, M. Zilk, V. Schuster, M. Zürch, T. Pertsch, C. Spielmann, J. Limpert, and J. Rothhardt, "Wavelength-scale ptychographic coherent diffractive imaging using a high-order harmonic source," Sci. Rep. **9**(1), 1735 (2019).
[121]B. Zhang, D. F. Gardner, M. D. Seaberg, E. R. Shanblatt, H. C. Kapteyn, M. M. Murnane, and D. E. Adams, "High contrast 3D imaging of surfaces near the wavelength limit using tabletop EUV ptychography," Ultramicroscopy **158**, 98–104 (2015).
[122]W. Eschen, C. Liu, D. S. Penagos Molina, R. Klas, J. Limpert, and J. Rothhardt, "High-speed and wide-field nanoscale table-top ptychographic EUV imaging and beam characterization with a sCMOS detector," Opt. Express **31**(9), 14212 (2023).
[123]Y. Jiang, J. Deng, Y. Yao, J. A. Klug, S. Mashrafi, C. Roehrig, C. Preissner, F. S. Marin, Z. Cai, B. Lai, and S. Vogt, "Achieving high spatial resolution in a large field-of-view using lensless x-ray imaging," Appl. Phys. Lett. **119**(12), 124101 (2021).
[124]D. Batey, C. Rau, and S. Cipiccia, "High-speed x-ray ptychographic tomography," Sci. Rep. **12**(1), 7846 (2022).
[125]M. Guizar-Sicairos, I. Johnson, A. Diaz, M. Holler, P. Karvinen, H.-C. Stadler, R. Dinapoli, O. Bunk, A. Menzel, J. Miao, P. Charalambous, J. Kirz, and D. Sayre, "High-throughput ptychography using eiger: Scanning x-ray nano-imaging of extended regions," Opt. Express **22**(12), 14859–14870 (2014).
[126]T. Harada, N. Teranishi, T. Watanabe, Q. Zhou, J. Bogaerts, and X. Wang, "High-exposure-durability, high-quantum-efficiency (>90%) backside-illuminated soft-x-ray CMOS sensor," Appl. Phys. Express **13**(1), 016502 (2020).
[127]R. M. Karl, G. F. Mancini, J. L. Knobloch, T. D. Frazer, J. N. Hernandez-Charpak, B. Abad, D. F. Gardner, E. R. Shanblatt, M. Tanksalvala, C. L. Porter, C. S. Bevis, D. E. Adams, H. C. Kapteyn, and M. M. Murnane, "Full-field imaging of thermal and acoustic dynamics in an individual nanostructure using tabletop high harmonic beams," Sci. Adv. **4**(10), eaau4295 (2018).
[128]K. Li, H. Lin, J. Niu, H. Xu, Y. Wang, C. Ke, X. Zhang, F. Zhang, J. Li, and Z. Fan, "Tabletop ptychographic imaging system with a 515 nm laser driven high-order harmonic source," Opt. Lasers Eng. **176**, 108105 (2024).

[129]N. J. Brooks, B. Wang, I. Binnie, M. Tanksalvala, Y. Esashi, J. L. Knobloch, Q. L. D. Nguyen, B. McBennett, N. W. Jenkins, G. Gui, Z. Zhang, H. C. Kapteyn, M. M. Murnane, and C. S. Bevis, "Temporal and spectral multiplexing for EUV multibeam ptychography with a high harmonic light source," Opt. Express **30**(17), 30331 (2022).
[130]N. Wiener, "Generalized harmonic analysis," Acta Mathematica **55**, 117–258 (1930).
[131]A. Khintchine, "Korrelationstheorie der stationären stochastischen Prozesse," Math. Ann. **109**, 604–615 (1934).
[132]V. Hilbert, A. Blinne, S. Fuchs, T. Feigl, T. Kämpfer, C. Rödel, I. Uschmann, M. Wünsche, G. G. Paulus, E. Förster, and U. Zastrau, "An extreme ultraviolet Michelson interferometer for experiments at free-electron lasers," Rev. Sci. Instrum. **84**(9), 095111 (2013).
[133]Y. Y. Li, Y. W. Lee, T. S. Ho, R. T. Wei, P. Y. Lai, K. S. Jao, I. C. Wu, S. H. Chen, and S. L. Huang, "Interferometry based EUV spectrometer," IEEE Photonics J. **9**(4), 1 (2017).
[134]Y.-Y. Li, Y.-W. Lee, T.-S. Ho, J.-H. Wang, I.-C. Wu, T.-W. Hsu, Y.-T. Chen, and S.-L. Huang, "Spectroscopic characterization of Si/Mo thin-film stack at extreme ultraviolet range," Opt. Lett. **43**(16), 4029–4032 (2018).
[135]H. Mashiko, M.-C. Chen, K. Asaga, A. Oshima, I. Katayama, J. Takeda, T. Nishikawa, and K. Oguri, "Spatially resolved spectral phase interferometry with an isolated attosecond pulse," Opt. Express **28**(14), 21025 (2020).
[136]S. Skruszewicz, A. Przystawik, D. Schwickert, M. Sumfleth, M. Namboodiri, V. Hilbert, R. Klas, P. Gierschke, V. Schuster, A. Vorobiov, C. Haunhorst, D. Kip, J. Limpert, J. Rothhardt, and T. Laarmann, "Table-top interferometry on extreme time and wavelength scales," Opt. Express **29**(24), 40333–40344 (2021).
[137]S. Fuchs, M. Wünsche, J. Nathanael, J. J. Abel, C. Rödel, J. Biedermann, J. Reinhard, U. Hübner, and G. G. Paulus, "Optical coherence tomography with nanoscale axial resolution using a laser-driven high-harmonic source," Optica **4**(8), 903 (2017).
[138]S. Fuchs, C. Rödel, A. Blinne, U. Zastrau, M. Wünsche, V. Hilbert, L. Glaser, J. Viefhaus, E. Frumker, P. Corkum, E. Förster, and G. G. Paulus, "Nanometer resolution optical coherence tomography using broad bandwidth XUV and soft x-ray radiation," Sci. Rep. **6**(1), 20658 (2016).
[139]M. Wünsche, S. Fuchs, S. Aull, J. Nathanael, M. Möller, C. Rödel, and G. G. Paulus, "Quasi-supercontinuum source in the extreme ultraviolet using multiple frequency combs from high-harmonic generation," Opt. Express **25**(6), 6936–6944 (2017).
[140]M. Wünsche, S. Fuchs, T. Weber, J. Nathanael, J. J. Abel, J. Reinhard, F. Wiesner, U. Hübner, S. J. Skruszewicz, G. G. Paulus, and C. Rödel, "A high resolution extreme ultraviolet spectrometer system optimized for harmonic spectroscopy and XUV beam analysis," Rev. Sci. Instrum. **90**(2), 023108 (2019).
[141]J. Nathanael, M. Wünsche, S. Fuchs, T. Weber, J. J. Abel, J. Reinhard, F. Wiesner, U. Hübner, S. J. Skruszewicz, G. G. Paulus, and C. Rödel, "Laboratory setup for extreme ultraviolet coherence tomography driven by a high-harmonic source," Rev. Sci. Instrum. **90**(11), 113702 (2019).
[142]A. J. Arikkatt, P. Wachulak, H. Fiedorowicz, A. Bartnik, P. Nyga, and K. Janulewicz, "Nanoscale optical coherence tomography using extreme ultraviolet radiation produced with a laser plasma source based on a gas puff target," Proc. SPIE **12502**, 1250207 (2022).
[143]K. A. Janulewicz, Ł. Węgrzyński, T. Fok, A. Bartnik, H. Fiedorowicz, S. Skruszewicz, M. Wünsche, E. Eckner, S. Fuchs, J. Reinhard, J. J. Abel, F. Wiesner, G. G. Paulus, C. Rödel, C. M. Kim, and P. W. Wachulak, "Broadband soft x-ray source from a clustered gas target dedicated to high-resolution XCT and x-ray absorption spectroscopy," Opt. Express **30**(26), 47867–47878 (2022).
[144]P. Wachulak, A. Bartnik, and H. Fiedorowicz, "Optical coherence tomography (OCT) with 2 nm axial resolution using a compact laser plasma soft x-ray source," Sci. Rep. **8**(1), 8494 (2018).
[145]S. Skruszewicz, S. Fuchs, J. J. Abel, J. Nathanael, J. Reinhard, C. Rödel, F. Wiesner, M. Wünsche, P. Wachulak, A. Bartnik, K. Janulewicz, H. Fiedorowicz, and G. G. Paulus, "Coherence tomography with broad bandwidth extreme ultraviolet and soft x-ray radiation," Appl. Phys. B **127**(4), 55 (2021).
[146]F. Wiesner, M. Wünsche, J. Reinhard, J. J. Abel, J. Nathanael, S. Skruszewicz, C. Rödel, S. Yulin, A. Gawlik, G. Schmidl, U. Hübner, J. Plentz, G. G. Paulus, and S. Fuchs, "Material-specific imaging of nanolayers using extreme ultraviolet coherence tomography," Optica **8**(2), 230 (2021).
[147]F. Wiesner, S. Skruszewicz, C. Rödel, J. J. Abel, J. Reinhard, M. Wünsche, J. Nathanael, M. Grünewald, U. Hübner, G. G. Paulus, and S. Fuchs, "Characterization of encapsulated graphene layers using extreme ultraviolet coherence tomography," Opt. Express **30**(18), 32267 (2022).
[148]J. J. Abel, J. Apell, F. Wiesner, J. Reinhard, M. Wünsche, N. Felde, G. Schmidl, J. Plentz, G. G. Paulus, S. Lippmann, and S. Fuchs, "Non-destructive depth reconstruction of Al-Al2Cu layer structure with nanometer resolution using extreme ultraviolet coherence tomography," Mater. Charact. **211**, 113894 (2024).
[149]F. Wiesner, J. J. Abel, M. Hussain, V. Krishna, A. R. Cadore, J. P. G. Felipe, A. M. Valencia, M. Wünsche, J. Reinhard, M. Gruenewald, C. Cocchi, G. G. Paulus, G. Soavi, and S. Fuchs, "Optical coherence tomography of van der waals heterostructures using extreme ultraviolet light," Adv. Mater. Interfaces **12**, 2400534 (2024).
[150]B. L. Henke, E. M. Gullikson, and J. C. Davis, "X-ray interactions: Photoabsorption, scattering, transmission, and reflection at E = 50-30,000 eV, Z = 1-92," At. Data Nucl. Data Tables **54**(2), 181–342 (1993).
[151]A. Bianconi, "Surface x-ray absorption spectroscopy: Surface EXAFS and surface XANES," Appl. Surf. Sci. **6**(3–4), 392–418 (1980).
[152]J. J. Abel, F. Wiesner, J. Nathanael, J. Reinhard, M. Wünsche, G. Schmidl, A. Gawlik, U. Hübner, J. Plentz, C. Rödel, G. G. Paulus, and S. Fuchs, "Absolute EUV reflectivity measurements using a broadband high-harmonic source and an in situ single exposure reference scheme," Opt. Express **30**(20), 35671 (2022).
[153]C. L. Porter, M. Tanksalvala, M. Gerrity, G. Miley, X. Zhang, C. Bevis, E. Shanblatt, R. Karl, M. M. Murnane, D. E. Adams, and H. C. Kapteyn, "General-purpose, wide field-of-view reflection imaging with a tabletop 13 nm light source," Optica **4**(12), 1552 (2017).
[154]P. S. Jørgensen, L. Besley, A. M. Slyamov, A. Diaz, M. Guizar-Sicairos, M. Guizar-Sicairos, M. Guizar-Sicairos, M. Odstrčil, M. Odstrčil, C. Detlefs, J. W. Andreasen, M. Holler, C. Detlefs, and J. W. Andreasen, "Hard x-ray grazing-incidence ptychography: Large field-of-view nanostructure imaging with ultra-high surface sensitivity," Optica **11**(2), 197–204 (2024).
[155]D. F. Gardner, B. Zhang, M. D. Seaberg, L. S. Martin, D. E. Adams, F. Salmassi, E. Gullikson, H. Kapteyn, M. Murnane, L. Sandberg, H. Jiang, J. A. Rodríguez, B. P. Fahimian, H. C. Kapteyn, J. Du, J. Miao, A. Nugent, G. J. Williams, J. N. Clark, A. G. Peele, M. A. Pfeifer, M. de Jonge, and I. McNulty, "High numerical aperture reflection mode coherent diffraction microscopy using off-axis apertured illumination," Opt. Express **20**(17), 19050–19059 (2012).
[156]A. de Beurs, L. Loetgering, M. Herczog, M. Du, K. S. E. Eikema, and S. Witte, "aPIE: an angle calibration algorithm for reflection ptychography," Opt. Lett. **47**(8), 1949 (2022).
[157]S. Senhorst, Y. Shao, S. Weerdenburg, R. Horsten, C. Porter, and W. Coene, "Mitigating tilt-induced artifacts in reflection ptychography via optimization of the tilt angles," Opt. Express **32**(25), 44017 (2024).
[158]I. Staude and J. Schilling, "Metamaterial-inspired silicon nanophotonics," Nat. Photonics **11**(5), 274–284 (2017).
[159]W. Bogaerts, D. Pérez, J. Capmany, D. A. B. Miller, J. Poon, D. Englund, F. Morichetti, and A. Melloni, "Programmable photonic circuits," Nature **586**(7828), 207–216 (2020).
[160]M. Du, L. Loetgering, K. S. E. Eikema, and S. Witte, "Ptychographic optical coherence tomography," Opt. Lett. **46**(6), 1337–1340 (2021).
[161]A. Rana, J. Zhang, M. Pham, A. Yuan, Y. H. Lo, H. Jiang, S. J. Osher, and J. Miao, "Potential of attosecond coherent diffractive imaging," Phys. Rev. Lett. **125**(8), 086101 (2020).
[162]S. Witte, V. T. Tenner, D. W. Noom, and K. S. Eikema, "Lensless diffractive imaging with ultra-broadband table-top sources: From infrared to extreme-ultraviolet wavelengths," Light Sci Appl **3**(3), 163 (2014).
[163]H. C. Strauch, F. Zhang, S. Mathias, T. Hohage, S. Witte, and G. S. M. Jansen, "Fast spectroscopic imaging using extreme ultraviolet interferometry," Opt. Express **32**(16), 28644 (2024).
[164]N. G. Orji, M. Badaroglu, B. M. Barnes, C. Beitia, B. D. Bunday, U. Celano, R. J. Kline, M. Neisser, Y. Obeng, and A. E. Vladar, "Metrology for the next generation of semiconductor devices," Nat Electron **1**(10), 532–547 (2018).
[165]D. Mamezaki, T. Harada, Y. Nagata, and T. Watanabe, "Imaging performance improvement of coherent extreme-ultraviolet scatterometry microscope with high-harmonic-generation extreme-ultraviolet source," Jpn. J. Appl. Phys. **56**(6S1), 06GB01 (2017).

[166]Y. W. Kim, D. G. Lee, S. Moon, C. M. Ku, J. H. Cho, and J. Ahn, "Actinic patterned mask imaging using extreme ultraviolet ptychography microscope with high harmonic generation source," Appl. Phys. Express **15**(7), 076505 (2022).
[167]F. Tuitje, W. Eschen, G. K. Tadesse, J. Limpert, J. Rothhardt, and C. Spielmann, "Reliability of ptychography on periodic structures," OSA Contin. **3**(6), 1691 (2020).
[168]C. L. Porter, T. Coenen, N. Geypen, S. Scholz, L. van Rijswijk, H.-K. Nienhuys, J. Ploegmakers, J. Reinink, H. Cramer, R. van Laarhoven, D. O'Dwyer, P. Smorenburg, A. Invernizzi, R. Wohrwag, H. Jonquiere, J. Reinhardt, O. El Gawhary, S. G. J. Mathijssen, P. D. Engblom, H. Chin, W. T. Blanton, S. Ganesan, B. J. Krist, F. Gstrein, and M. Phillips, "Soft x-ray: Novel metrology for 3D profilometry and device pitch overlay," Proc. SPIE **12496**, 124961I (2023).
[169]M. Hentschel, R. Kienberger, Ch. Spielmann, G. A. Reider, N. Milosevic, T. Brabec, P. Corkum, U. Heinzmann, M. Drescher, and F. Krausz, "Attosecond metrology," Nature **414**(6863), 509–513 (2001).
[170]S. Zayko, O. Kfir, M. Heigl, M. Lohmann, M. Sivis, M. Albrecht, and C. Ropers, "Ultrafast high-harmonic nanoscopy of magnetization dynamics," Nat. Commun. **12**(1), 6337 (2021).
[171]A. Zong, B. R. Nebgen, S.-C. Lin, J. A. Spies, and M. Zuerch, "Emerging ultrafast techniques for studying quantum materials," Nat Rev Mater **8**(4), 224–240 (2023).
[172]W. Eschen, S. Wang, C. Liu, R. Klas, M. Steinert, S. Yulin, H. Meißner, M. Bussmann, T. Pertsch, J. Limpert, and J. Rothhardt, "Towards attosecond imaging at the nanoscale using broadband holography-assisted coherent imaging in the extreme ultraviolet," Commun. Phys. **4**(1), 154 (2021).
[173]A. Ravasio, D. Gauthier, F. R. N. C. Maia, M. Billon, J.-P. Caumes, D. Garzella, M. Géléoc, O. Gobert, J.-F. Hergott, A.-M. Pena, H. Perez, B. Carré, E. Bourhis, J. Gierak, A. Madouri, D. Mailly, B. Schiedt, M. Fajardo, J. Gautier, P. Zeitoun, P. H. Bucksbaum, J. Hajdu, and H. Merdji, "Single-shot diffractive imaging with a table-top femtosecond soft x-ray laser-harmonics source," Phys. Rev. Lett. **103**(2), 028104 (2009).
[174]D. Gauthier, M. Guizar-Sicairos, X. Ge, W. Boutu, B. Carré, J. R. Fienup, and H. Merdji, "Single-shot femtosecond x-ray holography using extended references," Phys. Rev. Lett. **105**(9), 093901 (2010).
[175]R. L. Sandberg, D. A. Raymondson, C. La-o-vorakiat, A. Paul, K. S. Raines, J. Miao, M. M. Murnane, H. C. Kapteyn, and W. F. Schlotter, "Tabletop soft-x-ray Fourier transform holography with 50 nm resolution," Opt. Lett. **34**(11), 1618 (2009).
[176]G. K. Tadesse, W. Eschen, R. Klas, V. Hilbert, D. Schelle, A. Nathanael, M. Zilk, M. Steinert, F. Schrempel, T. Pertsch, A. Tünnermann, J. Limpert, and J. Rothhardt, "High resolution XUV Fourier transform holography on a table top," Sci. Rep. **8**(1), 8677 (2018).
[177]F. Zhang, B. Chen, G. R. Morrison, J. Vila-Comamala, M. Guizar-Sicairos, and I. K. Robinson, "Phase retrieval by coherent modulation imaging," Nat. Commun. **7**(1), 13367 (2016).
[178]A. L. Levitan, K. Keskinbora, U. T. Sanli, M. Weigand, and R. Comin, "Single-frame far-field diffractive imaging with randomized illumination," Opt. Express **28**(25), 37103–37117 (2020).
[179]X. Pan, C. Liu, and J. Zhu, "Single shot ptychographical iterative engine based on multi-beam illumination," Appl. Phys. Lett. **103**(17), 171105 (2013).
[180]P. Sidorenko and O. Cohen, "Single-shot ptychography," Optica **3**(1), 9 (2016).
[181]J. Barolak, D. Goldberger, B. Ivanic, D. Schmidt, C. A. M. Schrama, C. G. Durfee, and D. E. Adams, "Ultrafast, single-event ptychographic imaging of transient electron dynamics," Ultrafast Sci. **4**, 0058 (2024).
[182]F. Willems, S. Sharma, C. V. Korff Schmising, J. K. Dewhurst, L. Salemi, D. Schick, P. Hessing, C. Strüber, W. D. Engel, and S. Eisebitt, "Magneto-optical functions at the 3*p* resonances of Fe, Co, and Ni: *Ab initio* description and experiment," Phys. Rev. Lett. **122**(21), 217202 (2019).
[183]O. Kfir, S. Zayko, C. Nolte, M. Sivis, M. Möller, B. Hebler, S. S. P. K. Arekapudi, D. Steil, S. Schäfer, M. Albrecht, O. Cohen, S. Mathias, and C. Ropers, "Nanoscale magnetic imaging using circularly polarized high-harmonic radiation," Sci. Adv. **3**(12), eaao4641 (2017).
[184]Y. Sun, N. Liu, and Y. Cui, "Promises and challenges of nanomaterials for lithium-based rechargeable batteries," Nat. Energy **1**(7), 16071 (2016).
[185]A. Chatzimpinou, C. Funaya, D. Rogers, S. O'Connor, S. Kapishnikov, P. Sheridan, K. Fahy, and V. Weinhardt, "Dehydration as alternative sample preparation for soft x-ray tomography," J. Microsc. **291**(3), 248–255 (2023).
[186]T. Heuermann, Z. Wang, M. Lenski, M. Gebhardt, C. Gaida, M. Abdelaal, J. Buldt, M. Müller, A. Klenke, and J. Limpert, "Ultrafast Tm-doped fiber laser system delivering 1.65-mJ, sub-100-fs pulses at a 100-kHz repetition rate," Opt. Lett. **47**(12), 3095–3098 (2022).
[187]M. Kördel, A. Dehlinger, C. Seim, U. Vogt, E. Fogelqvist, J. A. Sellberg, H. Stiel, and H. M. Hertz, "Laboratory water-window x-ray microscopy," Optica **7**(6), 658 (2020).
[188]J. Reinhard, S. Kaleta, J. J. Abel, F. Wiesner, M. Wünsche, E. Seemann, M. Westermann, T. Weber, J. Nathanael, A. Iliou, H. Fiedorowicz, F. Hillmann, C. Eggeling, G. G. Paulus, and S. Fuchs, "Laboratory-based correlative soft x-ray and fluorescence microscopy in an integrated setup," Microsc. Microanal. **29**, 2014 (2023).
[189]G. Schneider, P. Guttmann, S. Heim, S. Rehbein, F. Mueller, K. Nagashima, J. B. Heymann, W. G. Müller, and J. G. McNally, "Three-dimensional cellular ultrastructure resolved by x-ray microscopy," Nat. Methods **7**(12), 985–987 (2010).
[190]G. McDermott, M. A. Le Gros, C. G. Knoechel, M. Uchida, and C. A. Larabell, "Soft x-ray tomography and cryogenic light microscopy: The cool combination in cellular imaging," Trends Cell Biol. **19**(11), 587–595 (2009).
[191]L. Rego, N. J. Brooks, Q. L. D. Nguyen, J. S. Román, I. Binnie, L. Plaja, H. C. Kapteyn, M. M. Murnane, and C. Hernández-García, "Necklace-structured high-harmonic generation for low-divergence, soft x-ray harmonic combs with tunable line spacing," Sci. Adv. **8**(5), 7380 (2022).
[192]L. Rego, K. M. Dorney, N. J. Brooks, Q. L. Nguyen, C. T. Liao, J. San Román, D. E. Couch, A. Liu, E. Pisanty, M. Lewenstein, L. Plaja, H. C. Kapteyn, M. M. Murnane, and C. Hernández-García, "Generation of extreme-ultraviolet beams with time-varying orbital angular momentum," Science **364**(6447), eaaw9486 (2019).
[193]M. Ossiander, M. L. Meretska, H. K. Hampel, S. W. D. Lim, N. Knefz, T. Jauk, F. Capasso, and M. Schultze, "Extreme ultraviolet metalens by vacuum guiding," Science **380**(6640), 59–63 (2023).